DEVELOPMENT OF A BIOMIMETIC HIP IMPLANT SYSTEM FOR DOGS USING ADDITIVE MANUFACTURING TECHNOLOGIES

A THESIS SUBMITTED TO
THE GRADUATE SCHOOL OF NATURAL AND APPLIED SCIENCES
OF
ANKARA UNIVERSITY

by

Mahmut Onur DEMİRAK

IN PARTIAL FULFILLMENT OF THE REQUIREMENTS
FOR THE DEGREE OF
MASTER OF SCIENCE
IN
BIOMEDICAL ENGINEERING

ANKARA
2024

ABSTRACT

MSc Thesis

DEVELOPMENT OF A BIOMIMETIC HIP IMPLANT SYSTEM FOR DOGS USING ADDITIVE MANUFACTURING TECHNOLOGIES

M. Onur DEMİRAK

Ankara University
Graduate School of Natural and Applied Sciences
Department of Biomedical Engineering

Supervisor: Prof. Dr. Pınar YILGÖR HURİ
Co-Supervisor: Prof. Dr. Kaan ORHAN

Degenerative changes in the hip joint of dogs lead to pain and restricted movement, negatively impacting their quality of life. In cases where treatment methods such as osteoarthritis management or femoral head osteotomy fall short, total hip arthroplasty emerges as a frequently preferred and successfully implemented procedure. Moreover, degenerative joint diseases like hip dysplasia is frequent in dogs, and can result in severe consequences such as difficulty in walking and chronic pain. Total hip replacement is regarded as an effective method in treating all these orthopedic issues. However, conventional methods used in veterinary implant production is challenging to create customized anatomically-shaped implants with surfaces with biological functionality, hindering bone adhesion and growth. The most frequently used method, machining on cast-produced implants, generally lack the ability to provide perfect anatomical fit with hindered biomimetic topography on the implant surface. Additive manufacturing technology, on the other hand, allows the creation of customized implants with complex and integrated lattice structures that enhances osseointegration. Therefore, additive manufacturing is an important design and production tool due to the design freedom it offers compared to traditional methods, enabling the production of implants with lattice surfaces and hip prosthesis components of various sizes with biomimetic properties. The aim of this thesis is to develop a total hip prosthesis system for dogs, designed with a trabecular surface to enhance osseointegration. Implants and lattice structures were designed, and structural tests were applied using finite element analysis methods on these structures. In vitro tests were performed to study the cytotoxicity of the manufactured metal implants and cell-material interactions. The findings of the study highlighted the mechanical and biological advantages of biomimetic design and production.

August 2024, 76 pages

Key Words: Additive Manufacturing; Biomimetic Design; Hip Implant System; Finite Element Analysis; Selective Laser Melting

ÖZET

Yüksek Lisans Tezi

EKLEMELİ İMALAT TEKNOLOJİLERİ İLE KÖPEKLER İÇİN BİYOMİMETİK TASARIMLI KALÇA İMPLANT SİSTEMİ GELİŞTİRİLMESİ

M. Onur DEMİRAK

Ankara Üniversitesi
Fen Bilimleri Enstitüsü
Biyomedikal Mühendisliği Anabilim Dalı

Danışman: Prof. Dr. Pınar YILGÖR HURİ
Eş Danışman: Prof. Dr. Kaan ORHAN

Köpeklerin kalça eklemindeki dejeneratif değişiklikler ağrıya ve hareket kısıtlılığına neden olarak yaşam kalitelerini olumsuz yönde etkilemektedir. Osteoartrit tedavisi veya femur başı osteotomisi gibi tedavi yöntemlerinin yetersiz kaldığı durumlarda, total kalça artroplastisi sıklıkla tercih edilen ve başarıyla uygulanan bir işlemdir. Ayrıca, kalça displazisi gibi dejeneratif eklem hastalıkları köpeklerde sık görülür ve yürüme güçlüğü, kronik ağrı gibi ciddi sonuçlara yol açabilir. Total kalça protezi tüm bu ortopedik sorunların tedavisinde etkili bir yöntem olarak kabul edilmektedir. Bununla birlikte, veterinerlik implant üretiminde kullanılan geleneksel yöntemler, kemik entegrasyonunu ve rejenerasyonunu teşvik eden, biyolojik işlevsellikte yüzeylere sahip, vakaya özel olarak tasarlanmış anatomik şekilli implantlar oluşturmak için önemli kısıtlar içermektedir. Veteriner hekimlikte kullanılan implantların üretiminde en sık kullanılan yöntem olan dökümle üretim ve yüzey işleme, genellikle implant yüzeyinde engebeli biyomimetik topografya ve anatomic yapıyla birebir uyumlu olmayan şekillerde üretim imkanı sunmaktadır. Eklemeli imalat teknolojisi ise, osteointegrasyonu artıran karmaşık ve entegre kafes yapılarına sahip özelleştirilmiş implantların oluşturulmasına olanak tanımaktadır. Bu nedenle eklemeli imalat, geleneksel yöntemlere göre sunduğu tasarım özgürlüğü nedeniyle, kafes yüzeyli implantların ve biyomimetik özelliklere sahip çeşitli boyutlarda kalça protezi bileşenlerinin üretilmesine olanak sağlaması nedeniyle önemli bir tasarım ve üretim aracıdır. Bu tezin amacı, köpekler için osteointegrasyonu artıracak trabeküler yüzeye sahip bir total kalça protez sistemi geliştirmektir. İmplantlar ve kafes yapılar tasarlanmış ve bu yapılar üzerinde sonlu elemanlar analiz yöntemleri kullanılarak yapısal testler uygulanmıştır. Üretilen metal implantların sitotoksisitesini ve hücre-malzeme etkileşimlerini incelemek için in vitro testler gerçekleştirilmiştir. Araştırmanın bulguları, biyomimetik tasarım ve üretimin mekanik ve biyolojik avantajlarını vurgulamaktadır.

Ağustos 2024, 76 sayfa

Anahtar Kelimeler: Eklemeli İmalat; Biyomimetik Tasarım; Kalça İmplant Sistemi; Sonlu Elemanlar Analizi; Seçici Lazer Eritme

FOREWORD AND ACKNOWLEDGEMENTS

First and foremost, I would like to express my deepest gratitude to my mentor and role model, Prof. Dr. Pınar YILGÖR HURİ, who has played a significant role in shaping my academic and professional interests from the moment she first lectured in my undergraduate years. It has been a great fortune, pride, and joy to feel her support behind me, and it will always be so.

I am deeply thankful to the MTE Lab team members Şeyda, Emre, Utku, Barış, Osama, Begüm, and Ayşe for their invaluable efforts and time spent on this journey. I hope to one day be able to show my appreciation for their contributions.

My heartfelt appreciation goes to the BTECH team, who will always hold a special place in my professional life and have greatly influenced the development of this work. Special thanks to my invaluable teammates Samet and Yüşa for believing in the dreams we built together and their vital contributions to this study.

I am immensely grateful to my dear wife, Serenay DEMİRAK, who stands foremost among all my life's achievement list and serves as the singular yet unwavering source of motivation for the continuation of that list.

Lastly, thanks to my father, Prof. Dr. Ahmet DEMİRAK, and my mother, Gülsüm DEMİRAK and my brother Hakan Erdem DEMİRAK who will undoubtedly be the happiest to see the completion of this work.

Mahmut Onur DEMİRAK
Ankara, August 2024

TABLE OF CONTENTS

LIST OF FIGURES

LIST OF TABLES

1. INTRODUCTION

Degenerative changes in the hip joint of dogs, such as hip dysplasia, often lead to pain and restricted movement, significantly impacting their quality of life. When conventional treatments like osteoarthritis management or femoral head osteotomy prove inadequate, total hip arthroplasty (THA) emerges as a frequently preferred and effective procedure performed by orthopedic surgeons. THA is considered one of the most effective clinical methods to alleviate joint pain and enable patients to return to a normal life, particularly for dogs suffering from severe degenerative joint diseases (Harasen, 2005).

Degenerative joint diseases, such as hip dysplasia, result in severe consequences including difficulty walking, chronic pain, and a significant decrease in quality of life for affected dogs. In these cases, total hip replacement is a recognized and effective treatment method (Fink et al., 2021). However, conventional methods used in implant production present challenges in creating surfaces with high biological functionality, which are essential for bone adhesion and growth. Surfaces created through machining on cast-produced implants typically have simpler geometries compared to those achievable through additive manufacturing (Chen, Wang, & Liu, 2022).

Additive manufacturing technology, also known as 3D printing, has revolutionized the production of implants by enabling the creation of complex lattice structures and integrating lattice production where osseointegration occurs at high levels. One of the most advanced techniques in additive manufacturing is powder bed fusion (PBF), which uses a high-power laser or electron beam to fuse fine metal powders layer by layer to create a solid structure (Wang et al., 2021). This technology allows for the design and fabrication of intricate geometries that closely mimic natural bone structures, which is crucial for enhancing biological functionality and promoting bone integration (Rafi, Karthik, & Gong, 2022).

Lattice structures, characterized by their porous and interconnected geometry, play a significant role in this process by providing a scaffold that supports bone ingrowth and vascularization. These structures are essential in improving the stability and longevity of

implants. In the healthcare sector, materials commonly used in additive manufacturing include titanium alloys, cobalt-chromium alloys, and biocompatible polymers. These materials are chosen for their excellent mechanical properties, corrosion resistance, and biocompatibility, making them ideal for creating durable and functional implants (Zhang et al., 2024; Li et al., 2023).

Finite Element Analysis (FEA) is a computational method used to predict how a product reacts to real-world forces, vibration, heat, and other physical effects. By breaking down a complex structure into smaller, manageable parts, FEA allows for a detailed analysis of the mechanical behavior of materials and structures. This method is particularly valuable in the design and testing of implants, as it helps in optimizing the design for maximum strength and durability while minimizing material use (Reddy et al., 2024; Kumar et al., 2024).

This thesis aims to develop a total hip prosthesis system with a trabecular surface designed to enhance osseointegration for dogs. The study involves the design of implants and lattice structures, and the application of structural tests using finite element analysis methods. Additionally, in-vitro tests are conducted to examine the material and implant bioactivation. The findings of this study highlight the mechanical and biological advantages of biomimetic design and production, focusing on enhancing the effectiveness and functionality of total hip prostheses for dogs. The research emphasizes the importance of additive manufacturing technologies, such as powder bed fusion, and the use of advanced materials in creating orthopedic solutions that improve the quality of life for canine patient.

2. LITERATURE REVIEW

2.1 Causes and Indications for Hip Implants

Hip implants in dogs are primarily indicated for severe hip dysplasia, arthritis, and traumatic injuries that lead to irreparable damage of the hip joint. Hip dysplasia, a genetic condition often seen in large breed dogs, results in the malformation of the hip socket, causing joint instability, pain, and progressive arthritis (Huggard, Wicks, & Corfield, 2022). This condition is the most common reason for considering hip replacement surgery in canines (Corr, 2007). Arthritis, especially osteoarthritis, is another significant cause of hip deterioration in dogs (Kwananocha, Magré, Kamali, & Verseijden, 2024; Tomé, Alves Pimenta, Sargo, & Pereira, 2023).

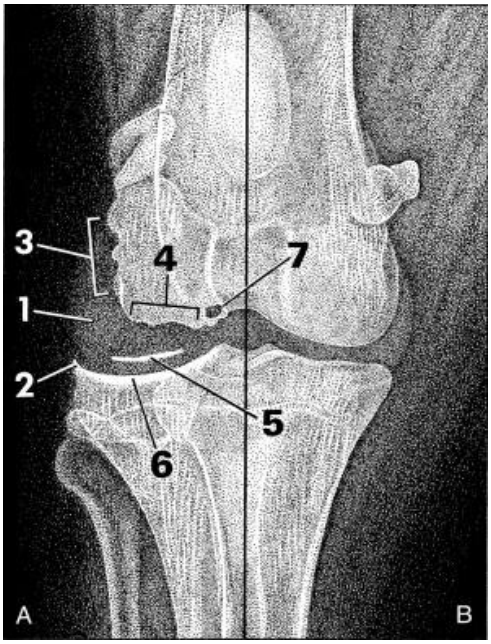

Figure 2.1 Radiographic indicators of joint disease (A) versus a normal joint (B) include several key changes. Commonly observed are an increased synovial mass (1), the presence of perichondral osteophytes (2), and the formation of enthesophytes (3). Less frequent seen are the erosion of the subchondral bone surface (4) and the appearance of joint mice (5). Signs indicative of chronic joint disease include increased opacity of the subchondral bone (6) and the formation of subchondral bone cysts (7). (Allan, G., & Davies, S. , 2018)

It involves the degeneration of joint cartilage, leading to pain, inflammation, and decreased mobility. Traumatic injuries, such as fractures or dislocations of the hip joint, may also necessitate the use of implants when conventional treatments fail to restore normal joint function (Kowaleski, & Dyce, 2004). The consequences of untreated hip joint issues in dogs can be severe, impacting their quality of life significantly. Chronic pain, lameness, and reduced mobility are common, leading to decreased activity levels and weight gain (Cason, 2014) This can further exacerbate joint problems and lead to a cycle of worsening health In severe cases, the dog may experience total loss of function in the affected limb, necessitating surgical intervention (Belshaw & Yeates, 2018).

2.2 Diagnosis

The diagnosis of hip joint issues typically involves a combination of clinical evaluation, imaging, and sometimes genetic testing. A thorough physical examination is conducted to assess pain, range of motion, and gait abnormalities. Radiographic imaging (X-rays) is the primary diagnostic tool used to visualize the hip joint structure, revealing abnormalities such as joint incongruity, subluxation, or degenerative changes (Figure 2.1) (Allan & Davies, 2018). Advanced imaging techniques like computed tomography (CT) or magnetic resonance imaging (MRI) can provide more detailed views when necessary (Andronescu, Kelly, & Kearney, 2015). In cases of hip dysplasia, genetic testing may be used to identify dogs at risk before clinical signs develop, enabling early intervention and breeding management to reduce the prevalence of this condition in future generations (Ginja, Silvestre, & Gonzalo-Orden, 2010).

2.3 Treatment Methods

Treatment options for hip joint issues in dogs vary depending on the severity and underlying cause. Conservative management includes weight control, physical therapy, pain management with non-steroidal anti-inflammatory drugs (NSAIDs), and joint supplements. These methods aim to reduce pain and improve joint function but are typically insufficient for severe cases (Kirkby & Lewis, 2012).

Surgical interventions become necessary when conservative treatments fail to provide adequate relief. The most common surgical options include:

- Femoral Head Ostectomy (FHO): This procedure involves the removal of the femoral head, allowing a false joint to form, which can alleviate pain but often results in reduced limb function (Anderson, 2011).

- Total Hip Replacement (THR, Figure 2.2): THR is the most definitive surgical treatment, involving the replacement of the entire hip joint with prosthetic components. This procedure restores normal joint function, alleviates pain, and improves mobility significantly. THR is a sophisticated surgical procedure increasingly used to treat severe hip joint disorders in dogs. It involves replacing the damaged hip joint with prosthetic components, effectively restoring function and alleviating pain. This procedure is particularly beneficial for dogs suffering from conditions such as hip dysplasia, osteoarthritis, and significant traumatic injuries that compromise the integrity and function of the hip joint (Huggard, Wicks, & Corfield, 2022).

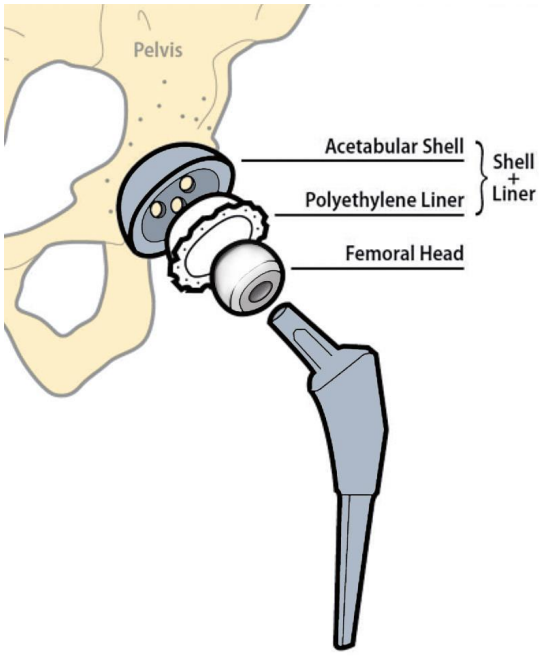

Figure 2.2 A schematic diagram illustrating a total hip replacement is shown, highlighting the various segments as defined by RSA (Radiostereometric Analysis) (Nebergall, 2015)

2.4 Indications for Total Hip Replacement (THR)

THR is primarily indicated for dogs with:

- **Severe Hip Dysplasia**: A congenital condition characterized by malformation of the hip joint, leading to instability, pain, and progressive arthritis (Hummel et al., 2020).
- **Advanced Osteoarthritis**: Degeneration of the hip joint cartilage, causing chronic pain, inflammation, and decreased mobility (Warnock et al., 2019).
- **Traumatic Injuries**: Significant fractures or dislocations of the hip joint that cannot be effectively managed through conservative treatments or less invasive surgical methods (Davidson et al., 2021).

The THR procedure involves several critical steps (Denny et al.,2018):

1. Preoperative Planning: Detailed radiographic and sometimes advanced imaging studies (such as CT or MRI) are performed to assess the hip joint's anatomy and plan the surgical approach. Proper sizing and selection of the prosthetic components are crucial for a successful outcome.
2. Anesthesia and Patient Preparation: The dog is placed under general anesthesia, and the surgical site is prepared aseptically. Proper anesthesia management is vital to ensure the patient's safety and comfort during the procedure.
3. Incision and Exposure: A surgical incision is made over the hip joint, and the surrounding muscles and tissues are carefully retracted to expose the hip joint.
4. Removal of the Damaged Joint: The femoral head and the damaged acetabulum are resected to prepare for the placement of the prosthetic components.
5. Insertion of Prosthetic Components: The acetabular cup is implanted into the pelvic bone, and the femoral stem is inserted into the femur. These components are typically made of biocompatible materials such as titanium or cobalt-chromium alloys, with a polyethylene liner to minimize friction.

6. Joint Reduction and Closure: The femoral head component is fitted into the acetabular cup, creating a new, functional hip joint. The surgical site is then closed in layers, and the dog is moved to recovery.

Recent advancements in THR include the development of biomimetic designs that mimic the natural bone structure, enhancing osseointegration and implant stability (Huri & Oto, 2022). Huri and Oto (2022) discuss the applications of 3D printing in veterinary medicine, highlighting its potential to improve surgical outcomes. Kwananocha, Verseijden, and Kamali (2024) spotlight a novel 3D-printed titanium implant designed for minimally invasive treatment of hip dysplasia in young dogs. Timercan, Brailovski, Petit, and Lussier (2019) present their research on personalized 3D-printed endoprostheses for limb sparing in dogs, focusing on modeling and in vitro testing.

2.5 Additive Manufacturing

Additive manufacturing (AM), commonly known as 3D printing, represents a transformative approach to producing three-dimensional objects through the layer-by-layer addition of materials based on digital models. This technology has found substantial applications across various industries due to its ability to create complex geometries that are otherwise difficult to achieve using traditional manufacturing techniques (Gibson et al., 2021).

One of the prominent branches of additive manufacturing is metal additive manufacturing, which has revolutionized the production of metal components with high precision and minimal material waste. Within this domain, Powder Bed Fusion (PBF) stands out, particularly the Selective Laser Melting (SLM) method (Figure 2.3). SLM employs a high-energy laser to selectively melt and fuse metal powder particles, layer by layer, to form a solid part (Kruth et al., 2010). This method is renowned for its ability to produce fully dense, high-performance metal parts with excellent mechanical properties (Herzog et al., 2016). In the medical field, SLM has demonstrated significant potential, particularly in the manufacturing of patient-specific implants and prosthetics. One of the primary advantages of SLM is its capability to produce complex, customized geometries

that conform precisely to the patient's anatomy. This customization enhances the fit and function of implants, reducing the risk of complications and improving patient outcomes (Sing et al., 2016). For instance, SLM has been used to create cranial and maxillofacial implants, which are critical in reconstructive surgeries following trauma or tumor removal (Lantada & Morgado, 2012).

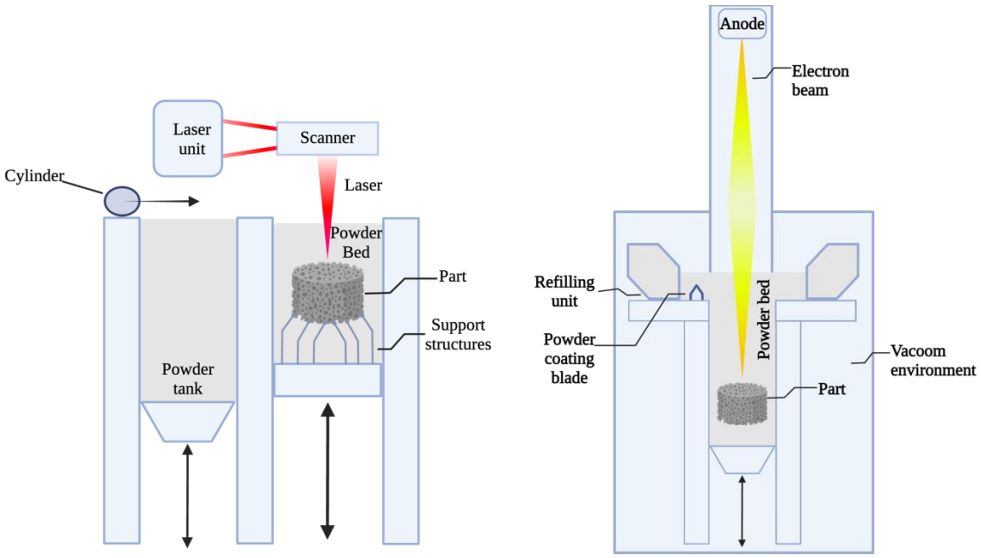

Figure 2.3 Schematic representation of selective laser melting (SLM, left) and electron beam melting (EBM, right) additive manufacturing methods (Demirak & Huri, 2023)

Furthermore, the biocompatibility of materials used in SLM, such as titanium and its alloys, makes them ideal for medical implants. These materials exhibit excellent corrosion resistance and mechanical properties, ensuring the longevity and reliability of the implants (Li et al., 2016). Additionally, SLM enables the fabrication of porous structures that promote osseointegration, where the implant integrates with the surrounding bone tissue, enhancing stability and functionality (Taniguchi et al., 2016). The veterinary field has also benefitted from the advancements in SLM technology. Like its applications in medicine, SLM is employed to create custom implants and prosthetics for animals, addressing unique anatomical and physiological needs. For example, SLM has been used to produce orthopedic implants for dogs and cats, offering a tailored solution for fractures, joint replacements, and other orthopedic conditions (Martins et al., 2019).

Moreover, SLM facilitates the creation of dental implants and prosthetics for animals, ensuring proper fit and function. This capability is particularly valuable for exotic pets and wildlife, where traditional implant options may be limited or unavailable (Leary et al., 2018). The precision and customization offered by SLM improve the overall quality of care and recovery for veterinary patients, enhancing their quality of life.

Electron Beam Melting (EBM) is a type of additive manufacturing technology that utilizes an electron beam as a heat source to selectively melt and fuse metal powders layer by layer to create complex, high-performance components (Figure 2.3). This method is particularly suited for producing parts made from metals and alloys with high melting points, such as titanium and its alloys, making it a valuable technology in industries like aerospace, medical implants, and automotive manufacturing (Gibson et al., 2021). In the medical field, EBM is used to produce custom orthopedic implants, such as hip and knee replacements, spinal implants, and dental implants. The technology allows for the creation of patient-specific implants with porous structures that promote bone ingrowth and improve the integration of the implant with the surrounding tissue (Harrysson et al., 2008).

2.6 Biomimetic Structures

In the realm of additive manufacturing, the concept of biomimetic structures is gaining considerable attention. Biomimetic structures are designs inspired by natural forms and processes, aiming to replicate the efficiency, functionality, and aesthetic of biological entities. These structures leverage the principles observed in nature to solve complex engineering challenges, offering innovative solutions in various fields, including aerospace, automotive, and biomedical engineering (Bar-Cohen, 2011). Biomimetic structures are engineered to mimic the hierarchical and multifunctional characteristics of biological systems. These structures often exhibit high strength-to-weight ratios, adaptability, and resilience. For example, the microstructures of bones and shells have inspired the development of lightweight yet sturdy materials in additive manufacturing. By mimicking these natural designs, engineers can create components that are not only strong and lightweight but also capable of withstanding dynamic loads and environmental

stressors (Vincent et al., 2006). One notable application of biomimetic structures is in the design of medical implants. Implants with biomimetic designs can closely resemble the mechanical properties of natural bone, promoting better integration with the surrounding tissue and reducing the risk of rejection or complications (Sun et al., 2018). Lattice structures are a subset of biomimetic designs that consist of repeating unit cells arranged in a periodic pattern. These structures can be tailored to achieve specific mechanical properties, such as stiffness, strength, and energy absorption. The type of lattice and its configuration play a crucial role in determining the overall performance of the material (Choy et al., 2019). Different types of lattices include:

Octet Truss Lattice (Figure 2.4): Known for its high stiffness and strength, making it suitable for load-bearing applications (Ashby, 2006) .

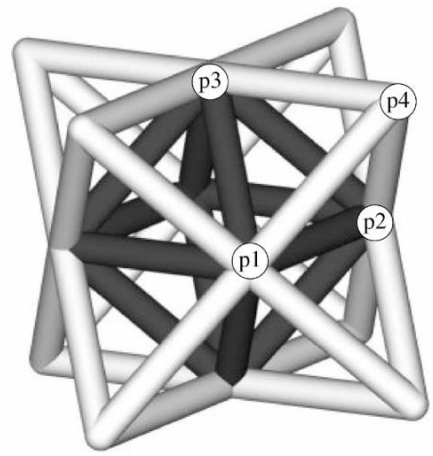

Figure 2.4 The structure of the octet-truss lattice material is illustrated, with darkened struts representing an octahedral cell. The nodes labeled p1–p4 form a tetrahedral cell. (Deshpande, 2001)

Gyroid Lattice (Figure 2.5): Exhibits excellent energy absorption characteristics, ideal for impact-resistant components (Maskery et al., 2018).

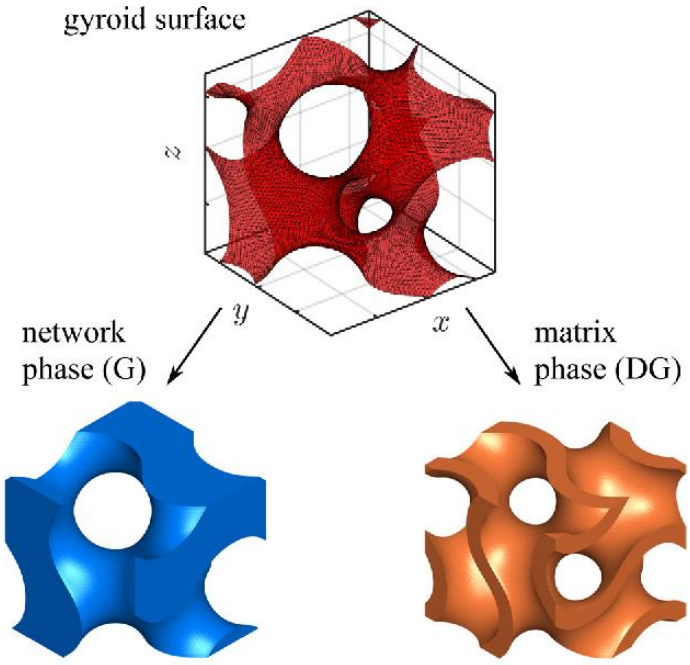

Figure 2.5 The TPMS gyroid surface (illustrated above) forms the network and matrix phase cells utilized in additive manufacturing

Voronoi Lattice: Mimics natural foam structures, offering a balance between stiffness and weight reduction (Zheng et al., 2014).

These lattice structures are extensively used in aerospace and automotive industries to create lightweight components without compromising structural integrity. In biological terms, these lattice structures can also mimic natural cellular formations found in bone, allowing for improved integration and interaction with biological tissues when used in medical implants (Choy et al., 2019). In addition to their mechanical properties, lattice structures can serve various biological functions. For example, they can be designed to facilitate cell growth and tissue integration, which is crucial in biomedical applications. The porosity of these structures allows for nutrient flow and waste removal, mimicking the natural environment of cellular tissues (Hollister, 2005). The effective elastic modulus of a material or structure is a measure of its stiffness, indicating how it deforms under applied stress. In the context of lattice structures, the effective elastic modulus is influenced by the geometry and arrangement of the unit cells. By carefully designing the lattice, engineers can tailor the stiffness of the material to meet specific requirements (Gibson & Ashby, 1997). For example, the effective elastic modulus of a gyroid lattice

can be adjusted by varying the thickness and orientation of its struts. This flexibility allows for the creation of materials with customized mechanical properties, suitable for applications ranging from flexible biomedical implants to rigid structural components (Maskery et al., 2018).

2.7 Finite Elements and Data Driven Design

Finite element analysis (FEA) is a computational method used to predict how materials and structures will respond to forces, deformation, and other physical effects. FEA divides a large system into smaller, simpler parts called finite elements. By solving the equations that describe these elements, FEA can simulate the behavior of the entire system under various conditions (Zienkiewicz et al., 2013). FEA is integral to additive manufacturing because it allows engineers to test and refine designs before physical production. This process helps identify potential issues, optimize material distribution, and ensure that the final product meets all performance requirements. For example, FEA is used extensively in the design of medical implants to ensure they can withstand the stresses and strains of the human body (Rajan et al., 2019). Static analysis is a subset of FEA that focuses on the response of structures under steady loads without considering time-dependent effects like inertia and damping. It involves calculating the displacements, strains, and stresses within a structure under constant loading conditions (Cook et al., 2012). In additive manufacturing, static analysis is crucial for evaluating the mechanical performance of complex structures. For instance, static analysis can be used to determine the load-bearing capacity of lattice structures and ensure they meet the necessary safety factors for their intended applications (Gibson et al., 2021). Homogenization is a mathematical method used to derive the macroscopic properties of a material from its microscopic structure. This technique simplifies complex materials, such as composites or porous structures, by averaging their properties over a representative volume element (Torquato, 2002). In the context of additive manufacturing, homogenization helps predict the effective mechanical properties of materials with intricate microstructures. This approach is particularly useful for materials designed with lattice structures, as it allows engineers to estimate their overall behavior based on the properties of individual unit cells (Gibson & Ashby, 1997). Topology optimization is a computational technique that determines the optimal material

distribution within a given design space to achieve the best performance under specified loading conditions. This method uses algorithms to iteratively remove inefficient material, resulting in a structure that is both lightweight and strong (Bendsøe & Sigmund, 2003).

In the medical field, topology optimization has significant applications in the design of implants and prosthetics. By optimizing the internal structure of these medical devices, engineers can enhance their mechanical properties while ensuring they are lightweight and comfortable for patients. Data-driven design leverages large datasets and advanced algorithms, such as machine learning and artificial intelligence, to inform and optimize the design process. By analyzing data from previous designs, simulations, and experimental results, engineers can identify patterns and insights that guide the development of new products (Raissi et al., 2019).

3. MATERIALS and METHODS

3.1 Materials

Materials used within the context of this study are listed in Table 3.1, involving their purpose of use and the companies they are provided from.

Table 3.1 Materials used, manufacturers and their intended use

Material	**Brand**	**Intended Use**
Adipose-derived stem cells (ASCs)	Isolated from human abdominal fat tissue	Isolated from human abdominal fat tissue
Fibroblast growth factor (bFGF)	Sigma-Aldrich	ASC expansion medium
High-glucose DMEM	Biological Ind.	ASC expansion medium
Fetal Bovine Serum (FBS)	Biological Ind.	ASC expansion & differentiation medium
Penicillin-Streptomycin (10X) Solution	Biological Ind.	ASC expansion & differentiation medium
L-Ascorbic acid	Serva	ASC differentiation medium
Sodium-β-glycerophosphate	Serva	ASC differentiation medium
Low-glucose DMEM	Biological Ind.	ASC differentiation medium
Dexamethasone	Merck	ASC differentiation medium
Trypsin	Biological Ind.	Cell passaging
Dimethyl Sulfoxide (DMSO)	Sigma-Aldrich	Cell freezing
Pierce™ Coomassie (Bradford) Protein Assay Kit	Thermo Fisher	Release kinetics analysis
Live/Dead™ Viability/Cytotoxicity Kit	Thermo Fisher	Cell viability analysis
Alamar Blue	Thermo Fisher	Cell viability analysis
Alexa Fluor 488 Phalloidin, DAPI	Thermo Fisher	Morphologic study
Alexa Fluor 594 Goat Anti-Rabbit IgG H&L	Abcam	Immunofluorescent staining

Table 3.1 Materials used, manufacturers and their intended use (continue)

Mouse Monoclonal Anti-CD31 antibody	Abcam	Vascularization analysis
Rabbit Polyclonal Anti-Osteopontin antibody	Abcam	Immunofluorescent staining
Alkaline Phosphatase Assay Kit (Colorimetric)	Abcam	Osteogenic differentiation analysis
Alizarin Red Staining Solution	Sigma-Aldrich	Calcium deposition analysis
Bovine Serum Albumin (BSA)	Sigma-Aldrich	Immunofluorescent staining
Triton X100	Merck	Cell permeabilization
Tween20	Merck	Cell permeabilization
Paraformaldehyde	Merck	Cell fixation
Ti64 Powder	BLT	Scaffold Production

3.2 Methods

3.2.1 Anatomical model acquisition

A digital and physical validation of the hip implant system, consisting of the cup and stem designs, as well as suitability for FEA studies, required the development of an anatomical model. The data obtained from the RATEM center specifically involved a dog diagnosed with osteoarthritis. Radiological images (309 slices of computed tomography) of a 4 years old male canine were obtained in DICOM format and 3D modeling stages were conducted using Materialise Mimics software (Figure 3.1) (Btech Innovation).

The steps followed while creating 3D anatomical model from DICOM data: Radiological images in DICOM format were imported into Materialise Mimics software. The characteristics of the imported data are 512x512 pixels with a slice thickness of 0.630 mm. The relevant anatomical structures, such as bones and joints, were segmented from the DICOM images using thresholding techniques. The selected threshold values were determined to be a minimum of 226 HU and a maximum of 2880 HU. A region growing algorithm was applied to refine the segmentation and accurately capture the anatomical

details. Using the Split Mask command, the pelvis, femur, and vertebrae were separated into distinct masks. The segmented images were then reconstructed into a 3D model by stacking the 2D slices and generating a surface mesh. The 3D model was smoothed and refined to eliminate any artifacts and ensure a high-quality representation of the anatomical structures. The final 3D anatomical model was exported in a suitable format (e.g., STL) for further use.

Using these steps, accurate 3D anatomical models were obtained. These models were subsequently used for validating the designs, conducting FEA studies, and 3D printing.

To gain an insight into the design of the acetabular cup and stem, certain measurements were taken on the 3D model.

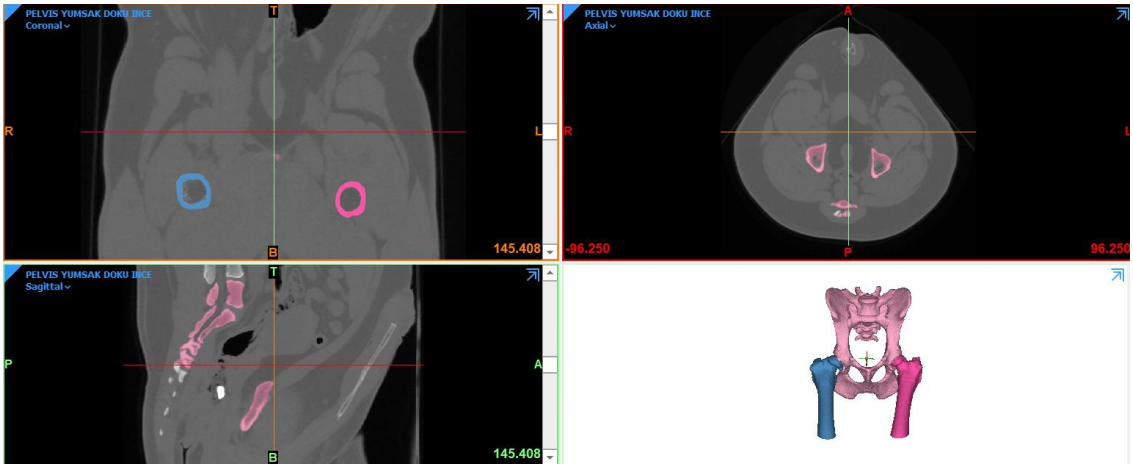

Figure 3.1 3D reconstruction of canine pelvis in Materialise Mimics

3.2.2 Acetabular cup design

The acetabular cup was designed to be a critical component of the hip implant system, ensuring a precise fit within the dog's hip joint. Fusion 2.0.18441 CAD software was employed during the design phase (Figure 3.2). The acetabular cup was designed as two bodies: the bulk structure representing the solid portion and the lattice structure representing the volumetric portion. These designs were carefully considered to ensure both structural integrity and optimal fit within the anatomical constraints of the dog's hip joint. The technical drawing of the acetabular cup is shown in the Figure 3.3.

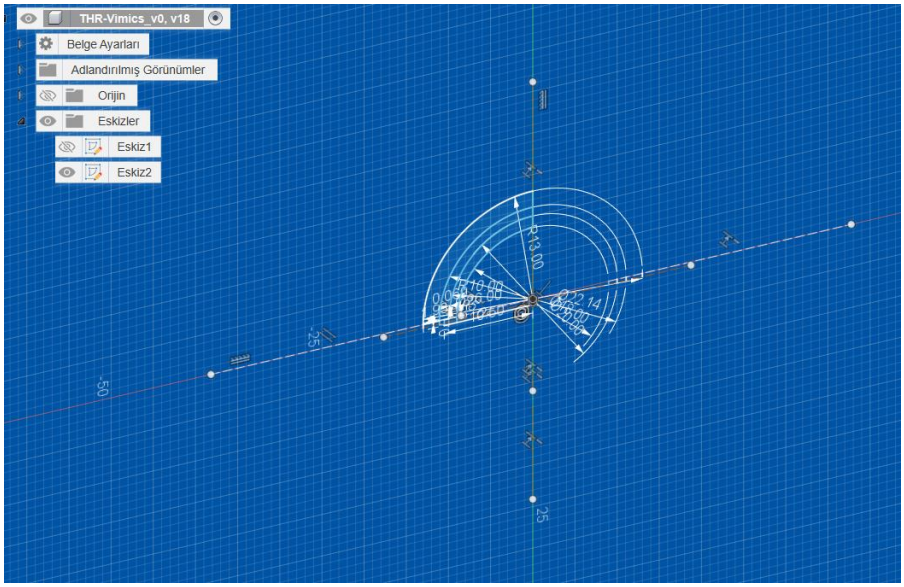

Figure 3.2 CAD design interface of THR system in Fusion360

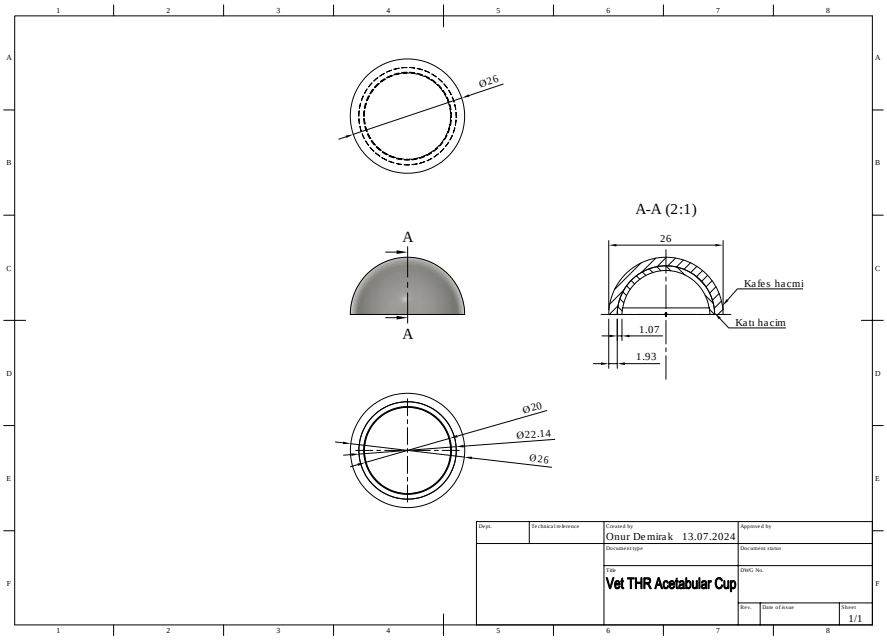

Figure 3.3 Acetabular cup technical drawing has been conducted in CAD software

3.2.3 Lattice design for acetabular cup and topologically optimized stem

In this study, different categories of lattice types, specifically Gyroid and Diamond, have been examined. The Gyroid lattice, which falls under the category of triply periodic

minimal surfaces (TPMS), and the Diamond lattice, which belongs to the graph-based category, were designed using nTop software.

3.2.4 Gyroid lattice

The TPMS gyroid lattice design was integrated into a cylindrical sample with the specifications shown in Table 3.3

Table 3.2 Gyroid lattice periodization parameters

Unit Cell Size (x, y, z)	3.86 mm
Approximate Thickness	0.4 mm
Orientation	UVW

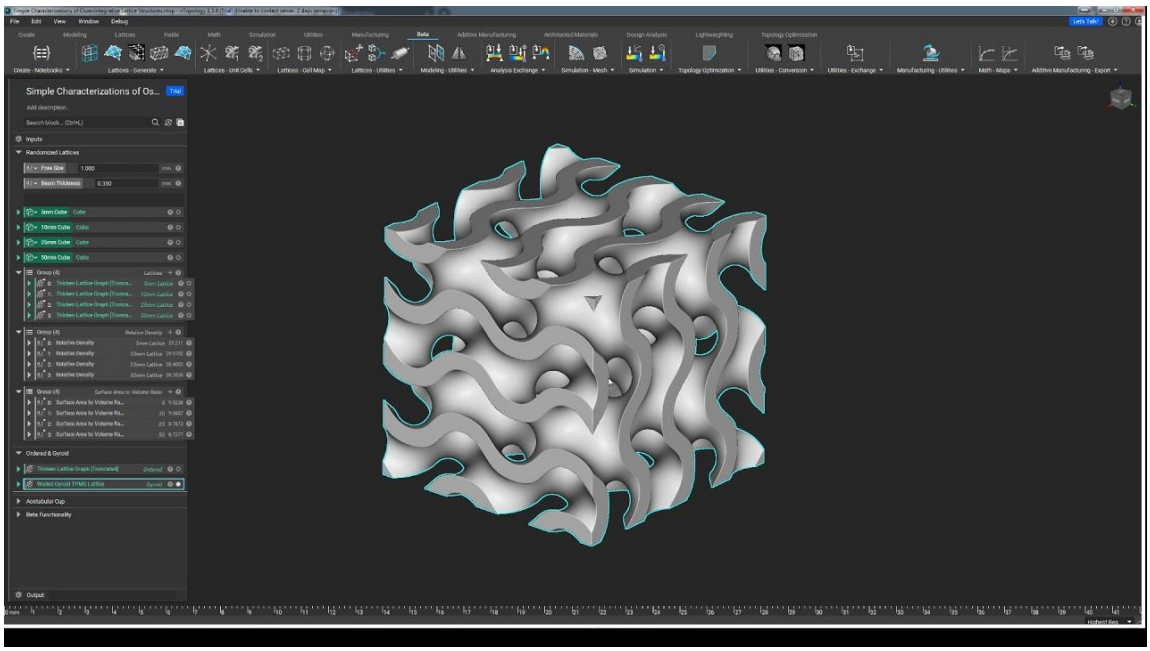

Figure 3.4 The gyroid unit cell lattice designed and periodized

The gyroid unit lattice shown in Figure 3.4, replicated throughout the cylindrical sample volume by creating a rectangular cell map, is illustrated in the figure. After application to the cylindrical sample, the total porosity was calculated to be 79.9%. To achieve the targeted porosity, the values for unit cell size and approximate thickness were determined

considering the constraints of additive manufacturing. These values were chosen to fall within the ranges known in the literature to provide optimal mechanical and biological performance for lattice structures.

3.2.5 Diamond lattice

The Diamond lattice design was integrated into the same cylindrical sample with the following specifications:

Table 3.3 Diamond lattice unut cell parameters

Unit Cell Size (x, y, z)	1.875 mm
Approximate Thickness	0.4 mm
Orientation	UVW

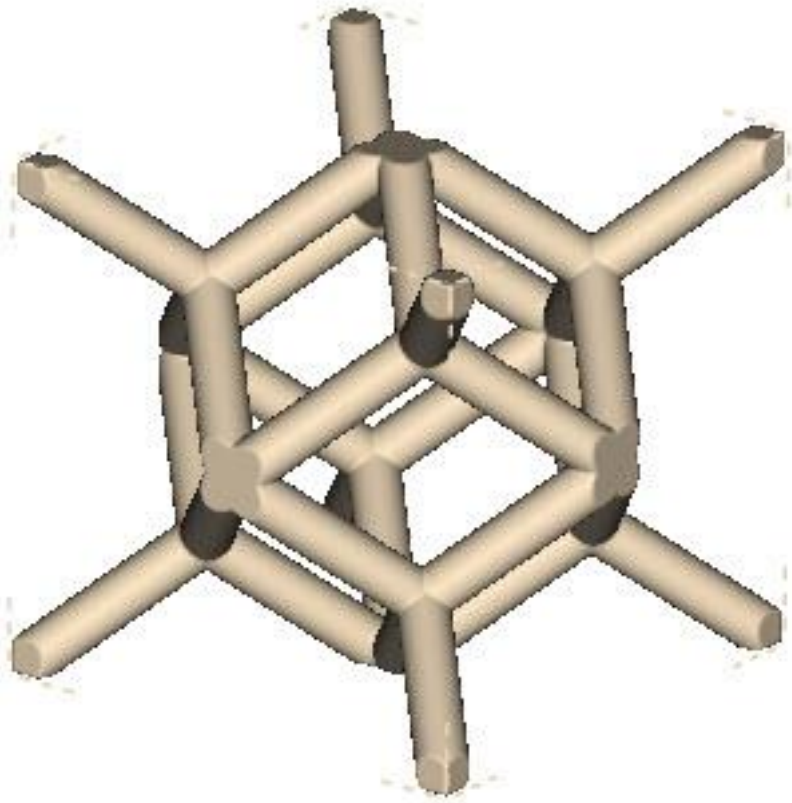

Figure 3.5 The diamond unit cell lattice implicit demonstration

The Diamond lattice shown in Figure 3.5 was designed and integrated following the same steps as the gyroid lattice, targeting the optimal ranges found in the literature. The resulting periodic lattice is illustrated in the figure. The porosity was calculated to be 80%.

3.2.6 Finite element analysis to lattices

The strength of the lattice structures integrated into the outer surface of the acetabular component, within the acetabulum, and on the topology-optimized stem's surfaces was evaluated using FEA methods. Plate designs were created around the samples with the integrated lattices, and a static loading scenario was established. However, due to the complex geometries of the lattice structures, the high number of mesh elements required for such an analysis necessitated a powerful processor. Consequently, a different approach was adopted for the finite element testing.

Using a technique called homogenization, strain loads were applied to the unit cells of the gyroid and diamond lattices in the X, Y, Z, XY, XZ, and YZ directions to calculate their effective mechanical properties. The effective properties obtained from this process were then used to derive new anisotropic material properties for the finite element analysis. The finite element analysis was subsequently performed by assigning these mechanical properties to the sample.

The FEA components were defined as the sample with effective elastic material properties assigned and plates made of stainless steel 316. The plates were designated as independent, and the lattice volume was designated as a dependent variable in the tie constraint block. As shown in the figure, the load conditions were set to 1100 N in the -Z direction. This value was derived from previous studies considering the average weight of a medium-sized dog. The calculation for determining the force is presented below:

Average Weight: A medium-sized dog weighing approximately 25 kg.

Peak Force: Using a conservative estimate of 3 times body weight for peak forces during activities such as running or jumping.

Force=25 kg×9.81 m/s2×3=735.75

Safety Factor: Applying a safety factor of 1.5.

Test Force=735.75 N×1.5≈1103.625

The result of the static analysis was recorded.

3.2.7 Biomimetic design integration for the acetabular cup

Biomimetic design principles were integrated into the design of the acetabular cup. The characteristics of natural bone structure and principles of structural optimization obtained from the literature were applied to the surface of the acetabular cup. This approach aimed to enhance the biocompatibility and mechanical strength of the implant. The integration process began by reviewing the relevant literature to identify key properties of natural bone, such as its pore size, porosity, and effective elastic modulus. These properties were then translated into design parameters in nTopology software. Two types of lattice structures were used as unit cells to create the biomimetic design. These are the Gyroid and Diamond structures. The Gyroid was specified as a TPMS lattice, while the Diamond belongs to beam-based graph structures.

3.2.8 Liner design

The liner component of the hip implant system was designed to ensure optimal compatibility between the acetabular cup and the femoral head. The design of the liner focused on minimizing friction and wear resistance to enhance the longevity and performance of the implant. Fusion 2.0.18441 CAD software was employed during the design phase.

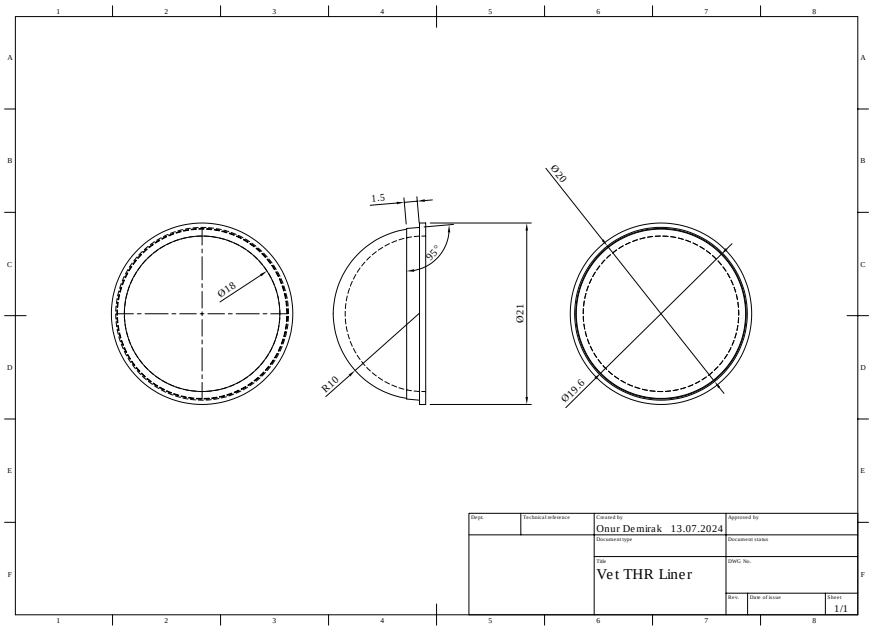

Figure 3.6 Technical drawing of the liner in CAD format

The liner was engineered to fit precisely within the acetabular cup while providing a smooth articulation surface for the femoral head. The drawing and model details of the liner design are specified in Figure 3.6.

3.2.9 Head design

The head component of the hip implant was designed to ensure a precise fit with the stem design. The design of the head aimed to maximize joint mobility and comfort by achieving a round and smooth surface. The drawing and model details of the head design are specified in Figure 3.7.

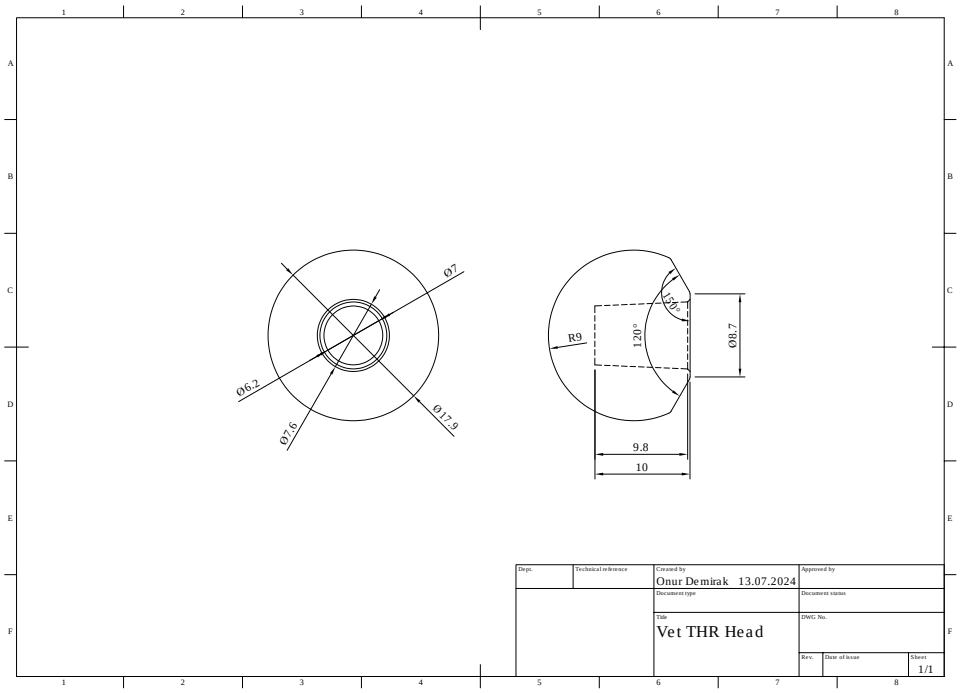

Figure 3.7 Femoral head component drawing in CAD

3.2.10 Stem design

The stem component is another critical part of the hip implant system, requiring a secure fit within the femur bone. The design of the stem aimed to ensure optimal fit and stability by considering the anatomical structure of the canine femur (Figure 3.8).

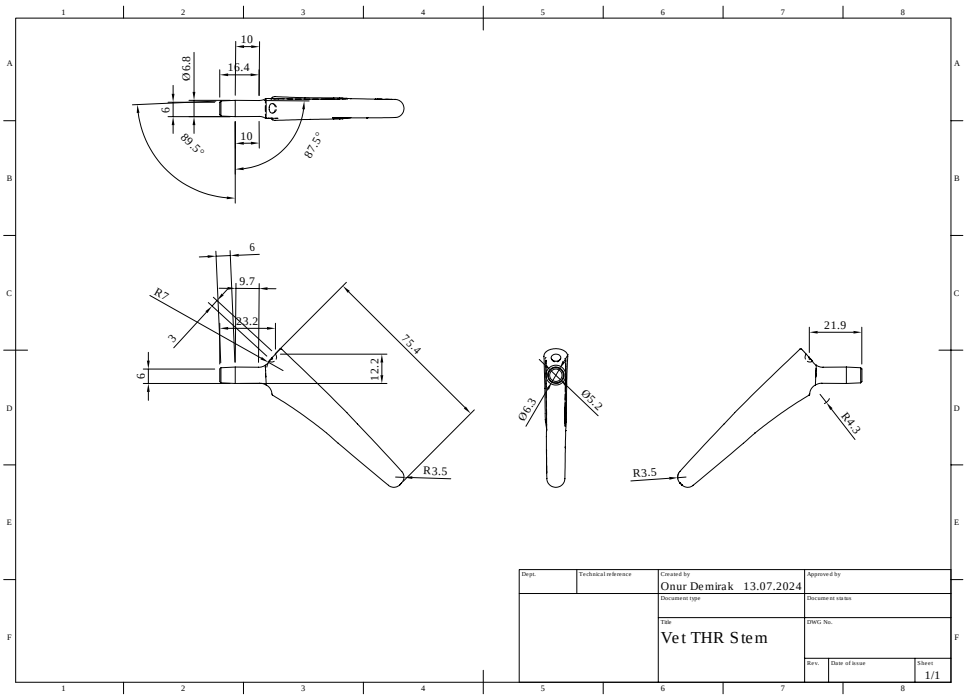

Figure 3.8 Stem component technical drawing

3.2.11 Topology optimization of stem component

The stem design was subjected to static analysis to observe the von Mises stress values. Initially, the femoral head, obtained during the anatomical modeling phase, was trimmed using the trim command in 3-matic software to comply with surgical techniques. Subsequently, the stem, designed to fit the femur dimensions, was placed inside the femur within the simulation environment. To enhance the usability of the analysis, the femur mesh was simplified and exported to nTop software along with the stem, ensuring the orientation was preserved.

The force surface was defined as the interface between the stem and the head, while the displacement restraint was set as the buccal surface of the trimmed femur, establishing the boundary conditions. A force of 1100 N, consistent with the value previously applied to the lattice structures and derived from the literature, was applied in the direction of the normal vector of the force surface. The material properties for the stem and femur were defined as:

Table 3.4 FE components (stem and femur) isoelastic properties

FE Component	Elastic Modulus	Poisson Ratio
Stem	113.8 GPa	0.342
Femur	16.7 GPa	0.3

The analysis results were recorded, and the von Mises stress values on the stem were saved as a point cloud.

To apply data-driven design principles, the von Mises stress values were defined as a field in nTop software, and each von Mises value (total of 94,789 points) was processed using a mathematical operation called the ramp function. The ramp function maps numbers within a specific range to another desired range. The input minimum and maximum values were set based on the minimum and maximum values observed in the von Mises point map, representing the points of minimum and maximum stress. The output values were parametrically defined according to the cell size of the desired lattice type, as follows:

Cell Type: TPMS Gyroid
Min Cell Size: 1.29 mm
Max Cell Size: 7.72 mm
Approximate Thickness: 0.4 mm

Using the resulting values, the design aimed to have a larger pore size (maximum cell size) in areas of minimum stress and a more bulk structure (minimum cell size) in areas of maximum stress.

After applying data-driven design to the stem based on the results of the topology optimization, the optimized stem was subjected to the same static analysis scenario and load conditions as the bulk stem. The results were recorded for comparison.

3.2.12 Sample production

Gyroid and Diamond structures were produced using a BLT SLM machine and Arcam A2X EBM machine according to the specified design parameters. Considering the examples in the literature where the Arcam A2X EBM machine and BLT slm machine are used, the production parameters determined for the devices are shown in Table 3.5 and Table 3.6. It is known that due to the EBM process being sensitive to parameter changes, it does not provide as much flexibility to the user in this context compared to SLM.

Table 3.5 EBM process parameters

Beam Current	15mA
Line Offset	0.2mm
Focus Offset	25mA
Manual Speed	4530mm/s
Grid Voltage	60000V

Table 3.6 SLM process parameters

Laser power	100 W
Scannin speed	600 mm/s
Layer thickness	30 μm
Hatch distance	60

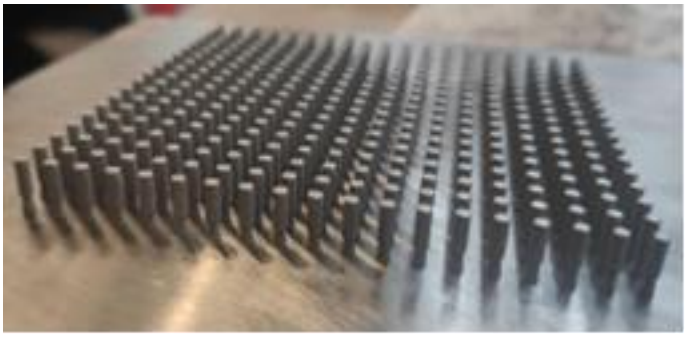

Figure 3.9 Samples fabricated by selective laser melting and electron beam melting

3.2.13 In vitro testing

3.2.14 Indirect cytotoxicity test

In order to determine the cytotoxicity of the materials used, indirect cytotoxicity tests were carried out in accordance with the MEM-extraction test specified in 10993/EN 30993. Based on the microscopic data obtained in accordance with the cytotoxicity test, scoring is made according to the evaluation criteria given in Table 3.7. According to this table, the grades obtained from the first three criteria (spread of the cell layer, amount of dead cells and change in cell morphology) are averaged. This average grade is then added with the grade from the last criterion (cell growth inhibition) to obtain the final cytotoxic response index value, ranging from 0 to 8 as presented in Table 3.8**.** This value is used to evaluate whether the material is cytotoxic.

Table 3.7 Cytotoxicity test evaluation criteria

	Evaluation Criteria	Grade
Spread of The Cell Layer (Confluency)	100%	0
	90-100%	1
	60-90%	2
	30-60%	3
	0-30%	4
Amount of Dead Cells	Never seen	0
	0-5%	1
	5-10%	2
	10-20%	3
	≥ 20%	4
Change in Cell Morphology	No change observed	0
	Little change, few cells affected	1
	Moderate change, some cell morphology changed	2
	Moderate change, change in morphology of many cells	3
	High level of change, change in morphology of all cells observed	4
Cell Growth Inhibition	0-10%	0
	10-30%	1
	30-50%	2
	50-70%	3
	70-100%	4

Table 3.8 Cytotoxic response index and cytotoxicity assessment

Cytotoxic Response Index	Reactivity	"Material is Cytotoxic"
0-1	No	No
1-3	Little	No
3-5	Middle	should be reevaluated
5-7	More	Yes
7-8	A lot	Yes

Samples were sterilized by exposure to UV light (400 nm) for 30 min prior to the tests. UHMWPE was used as the positive control and Latex was used as a negative control since it was known to have a cytotoxic effect (Baek et al., 2005). Cell culture medium was used as the extraction fluid (10% FBS and 1% P/S in 89% high glucose DMEM). Samples were added to 5 mL of extraction media and kept under continuous shaking at 60 rpm for 24 h in 15 mL falcon tubes.

L929 cells were transferred into T75 flasks in cell culture medium (10% FBS and 1% P/S in 89% high glucose DMEM). It was cultured in an incubator at standard culture conditions (37 ^{o}C, 5% CO_2 and humidity) for 24 h. Cells were seeded in 24-well cell culture dishes at a concentration of 5000 cells/cm^2. When the cells cultured under standard culture conditions in a CO_2 incubator for 24 hours became approximately 70% confluent, morphological evaluations were made with an inverted light microscope (Zeiss Primovert Inverted, Germany) and then the extraction liquids were added to the cell plates at 1000 µL/well.

Extraction liquids obtained from the samples were added to the cell monolayer in triplicates for each group. At 24 and 48 hours after the addition of the extraction liquids, the confluency of the cell layer and the changes in the cell morphology were evaluated by microscopic examination. The data obtained from the microscopic examination were compared with the positive and negative control groups and graded according to the evaluation criteria given in Table 3.3. Grades obtained from the first three criteria (spread

of the cell layer, amount of dead cells and change in cell morphology) were averaged. This average grade was added to the grade obtained from the last criterion (cell growth inhibition) and used to obtain the final cytotoxic response index value ranging from 0 to 8 (Table 3.4). This value was used to evaluate whether the produced material was cytotoxic.

3.2.15 Cell seeding and culture

To study the interaction between metal lattice samples and preosteoblast cells (MC3T3), cell seeding was conducted on the samples. Two cell seeding methods were employed on gamma-sterilized samples: (1) direct cell seeding on metal samples and (2) cell seeding within a fibrin gel. A total of 20 samples, 10 for each geometry, were seeded with MC3T3 cells (passage 12) at a density of 200,000 cells per sample. Post seeding, the samples were cultured in proliferation medium (a-MEM high glucose, 10% fetal bovine serum, 1% P/S) for the initial 3 days and then in osteogenic differentiation medium from days 3 to 14.

The number of viable cells on the samples was measured using the Cell Titer assay on days 3, 7, and 14 of culture. For this, the samples were incubated with Cell Titer solution in phenol red-free DMEM medium (5% v/v) under standard cell culture conditions for 1 hour. Post incubation, 200 µL of the test solution was transferred to 96-well plates, and the absorbance values were recorded using an ELISA reader. Additionally, on days 7 and 14 of culture, the samples were fixed at 4°C for 4 hours using a 3.7% paraformaldehyde solution for further analysis.

3.2.16 Morphological analysis

The samples fixed on days 7 and 14 of the culture were analyzed using scanning electron microscopy (SEM). Following fixation, the samples underwent dehydration through sequential washing with ethanol solutions of increasing concentrations (30%, 50%, 70%, and 100% v/v) and were then allowed to air dry at room temperature. Once dried, the samples were mounted on stubs using double-sided conductive carbon tape. The surfaces

of the mounted samples were then sputter-coated with gold at the METU Central Laboratory. Imaging was performed using a Quanta 400F Field Emission SEM.

3.2.17 Immunofluorescence staining

The samples, fixed on days 7, 14, and 21 of the culture, were washed three times with PBS for 30 minutes each time. Immunofluorescence staining was carried out using an Anti-Osteopontin antibody (Abcam ab8448, mouse) and DAPI. To prevent non-specific binding and permeabilize cell membranes, the samples were incubated in PBS containing 0.2% Triton-X-100 and 1% Bovine Serum Albumin (BSA) for 2 hours at 4°C. After blocking and permeabilization, the samples were incubated overnight at 4°C with the primary antibody diluted in PBS with 1% donkey serum. Subsequently, the samples were incubated with a secondary antibody for 3 hours at room temperature. CyTM3-conjugated donkey anti-mouse IgG served as the fluorophore-conjugated secondary antibody. The samples were then examined using both a fluorescence microscope and a confocal microscope. Confocal imaging was conducted using a Zeiss LSM 880 microscope, with the following excitation/emission values: Alexa Fluor 594: 590/618 nm; DAPI: 461/358 nm.

3.2.18 Alkaline phosphatase activity assay

The activity of the alkaline phosphatase (ALP) enzyme was assessed using an ELISA kit from Abcam. To begin, cells on the samples were lysed through a process involving washing, freeze-thaw cycles, and probe sonication. After centrifugation to eliminate cell debris and other unwanted components, the supernatant was incubated with 40 µL of p-nitrophenyl phosphate (pNPP) substrate in a 96-well plate at 37°C for 15 minutes. The reaction was halted by adding 80 µL of 0.5N stop solution. Absorbance was then measured at 405 nm using a plate reader. ALP enzyme activity in the samples was quantified using a standard curve generated with known concentrations of pNPP provided in the kit.

3.2.19 Statistical analysis

All quantitative results are presented as mean ± standard deviation (n=3). The data were analyzed based on one-way analysis of variance (ANOVA), considering p-values less than 0.05 as statistically significant. Tukey's test was used for determining the significance of differences between multiple groups, while t-tests were employed for other cases. The statistical analyses were performed using GraphPad Prism 6.0 software.

4. RESULTS AND DISCUSSION

4.1 Anatomical Model Acquisition

The anatomical modeling of the canine resulted in three separate 3D models that meet anatomical expectations: two femurs and a pelvis (Figure 4.1). The measurements obtained from these models, which will be used in subsequent studies, are shown in the Figure 4.2. The acetabular hole diameter has been measured as 24 mm. The angle of the femur was nearly 120˚ and the femoral head distance to imaginary stem was almost 24 mm with the length of 50 mm.

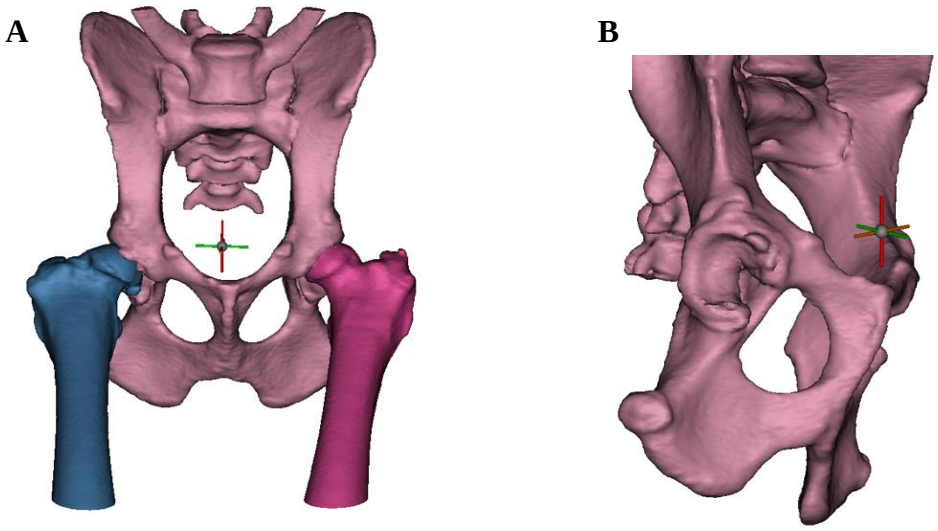

Figure 4.1 (A) 3D anatomical models of femurs and pelvis (B) Anatomical geometry of acetabulum

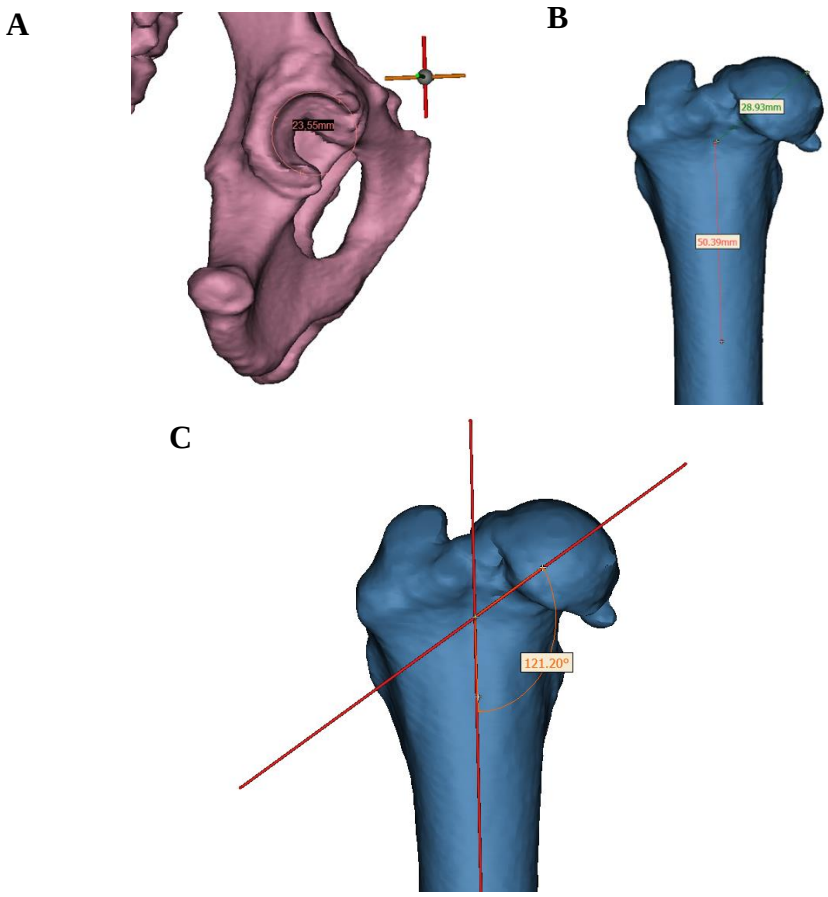

Figure 4.2 Measurements obtained from 3D models: (A) Acetabular diameter (B) Femoral blueprints for stem design (C) Femoral angle

4.2 THR Components Design

The 3D models of the total hip replacement components (acetabular cup, head, liner, and stem) designed according to the anatomical data of the dog are as follows (Figure 4.3).

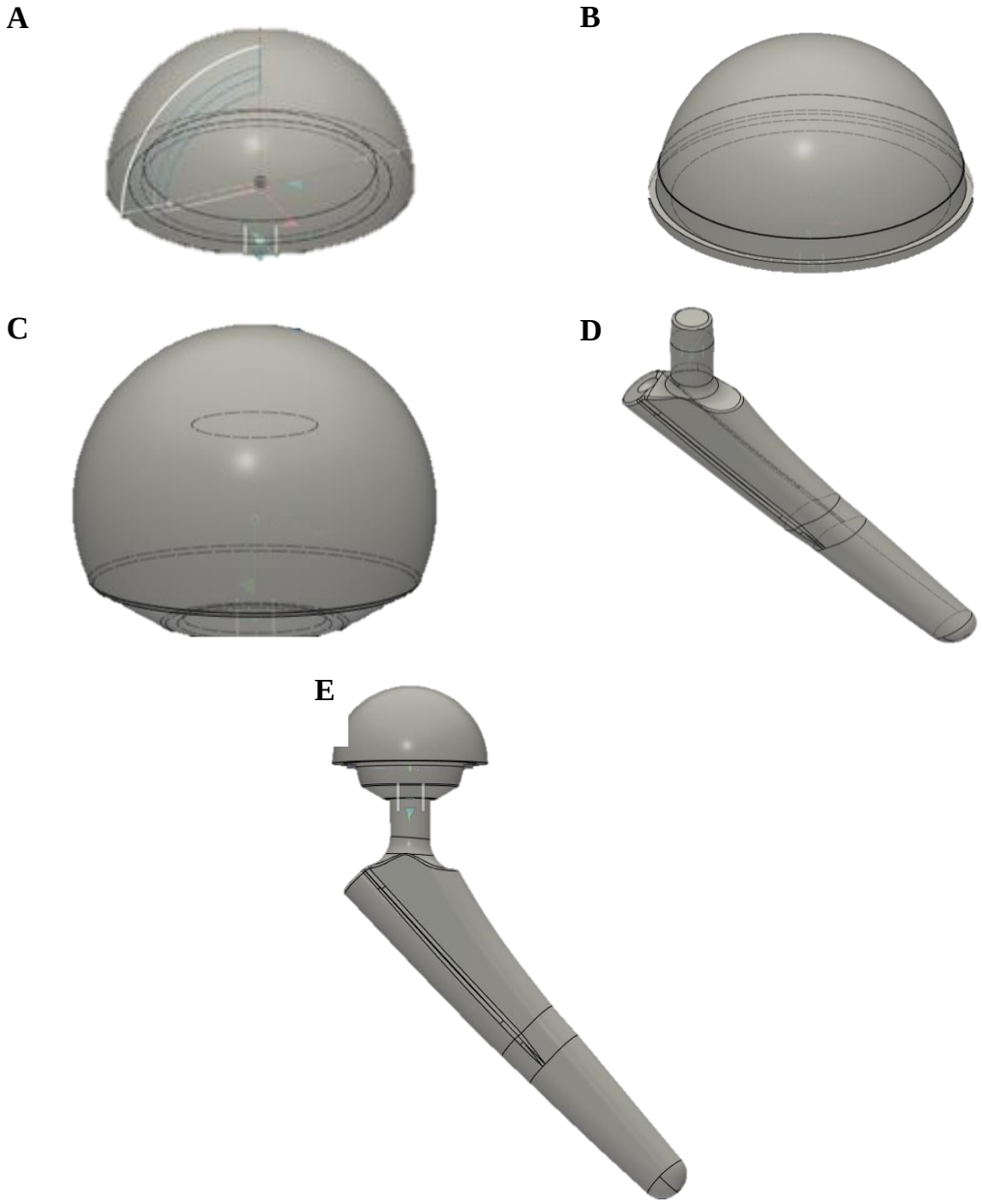

Figure 4.3 Total hip replacement system: (A) Bulky acetabular cup (B) Liner (C) Head (D) Stem (E) The system assembly

4.3 Lattice Design and FEA

The gyroid and diamond lattice structures were applied to the experimental samples, resulting in the geometries shown in Figure 4.4. The intended porosity (80%) was achieved in both samples.

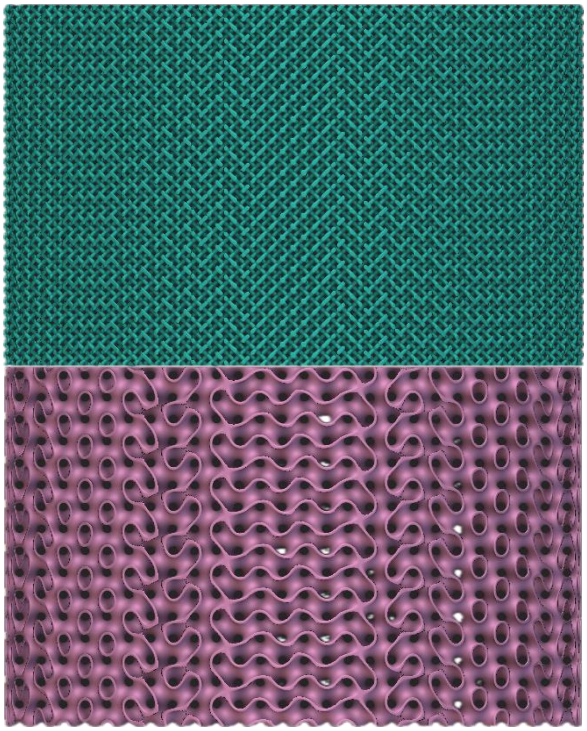

Figure 4.4 Diamond (left) and Gyroid (right) applied cylindric samples

After the initial setup for the FEA, the boundary conditions are depicted in Figure 4.5

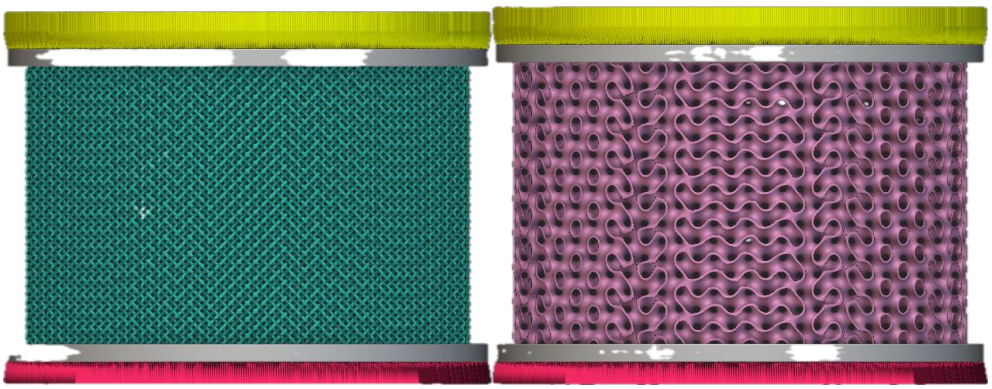

Figure 4.5 Boundary conditions force (yellow) and displacement restraint (pink) applied

To enable FEA of the lattice structures, a homogenization method was employed. This process yielded two types of results: displacement homogenization and directional homogenization. Homogenization is a technique used to approximate the macroscopic properties of a material with a complex microstructure, such as a lattice, by averaging its properties over a representative volume element. This method simplifies the computational model while retaining the essential characteristics of the material's behavior.Displacement Homogenization (Table 4.1) is the approach focuses on determining the overall deformation behavior of the lattice structure under applied loads. By averaging the displacements of the microstructure, it provides an effective means to model the global mechanical response of the lattice material. Directional Homogenization (Table 4.2) is the method calculates the effective mechanical properties in specific directions, considering the anisotropic nature of the lattice. It aids in understanding how the material behaves differently along various axes, which is crucial for accurately predicting the performance of lattice structures under different loading conditions.

Table 4.1 Displacement homogenization results

Sample	Displacement homogenization	Displacement homogenization (z-axis scaled)	Displacement color map
Diamond	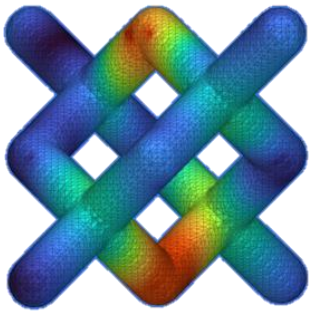	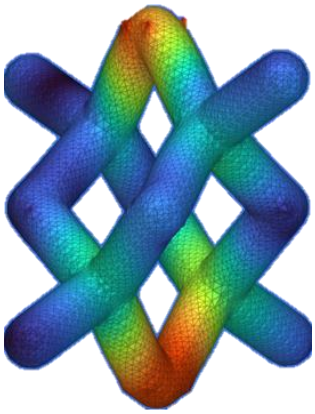	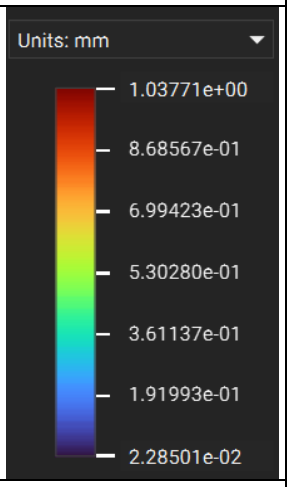
Gyroid	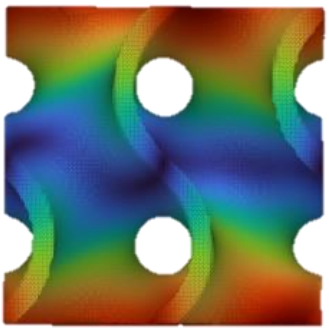	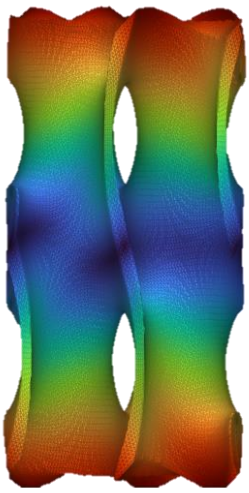	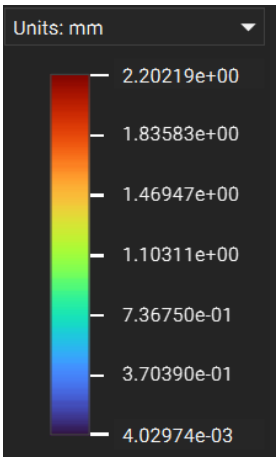

Table 4.2 Directional homogenization results

Sample	Directional homogenization	Colormap
Diamond	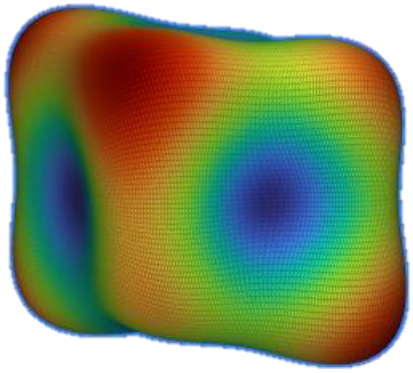	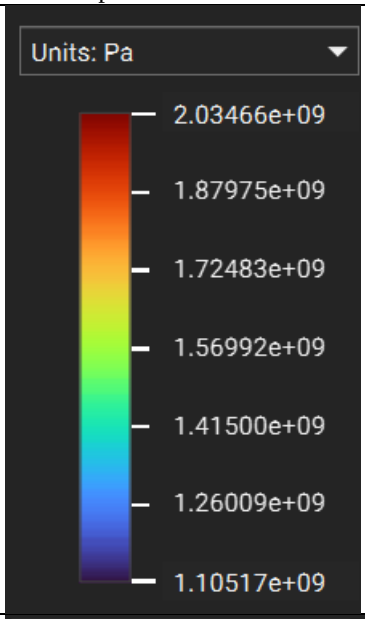
Gyroid	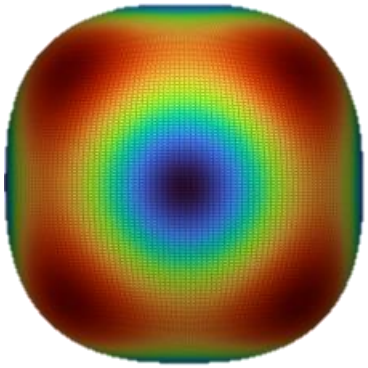	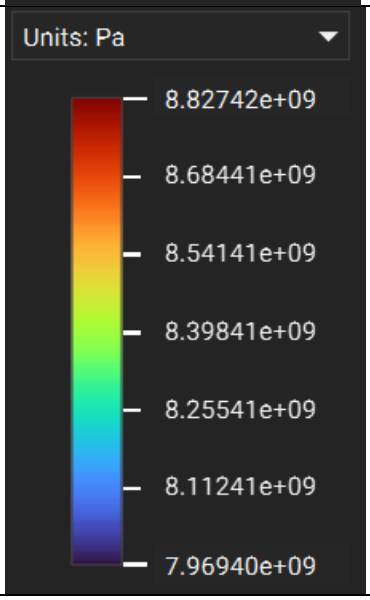

Focusing on the homogenization results of the gyroid lattice:

Degree of Freedom (DoF) Count: The analysis involved 2,209,191 degrees of freedom, indicating the complexity and detail of the model.

Element Count: A total of 455,444 elements were used in the finite element mesh, providing a refined representation of the lattice structure.

Node Count: The model comprised 736,397 nodes, which are the points at which the elements are connected.

Relative Density: The relative density of the gyroid lattice was found to be 0.1997, reflecting the proportion of solid material within the lattice structure.

Zener Ratio: The Zener ratio was calculated as 1.1227, indicating the degree of anisotropy in the elastic properties of the lattice.

These properties were obtained from the analysis.

Another key outcome of the analysis is the effective elastic modulus, which measures the stiffness of the material under uniaxial stress. This value is crucial for understanding the mechanical performance of the lattice structure.

To determine the effective elastic modulus, an elasticity matrix was obtained. The elasticity matrix (also known as the stiffness matrix, Table 4.3) describes the material's response to stress in multiple directions, encapsulating the relationship between stress and strain in the material. It provides a comprehensive representation of the material's elastic properties, essential for accurate mechanical modeling.

Table 4.3 Gyroid unit cell elasticity matrix

1.18978e+10	**5.91482e+09**	**5.91474e+09**	**6.42017e+06**	**1.44192e+06**	**1.43257e+06**
5.91482e+09	1.18978e+10	5.91472e+09	1.14988e+06	6.62046e+06	1.55696e+06
5.91474e+09	5.91472e+09	1.18974e+10	1.3533e+06	1.4095e+06	6.8103e+06
6.42017e+06	1.14988e+06	1.3533e+06	3.35847e+09	467168	479265
1.44192e+06	6.62046e+06	1.4095e+06	467168	3.35842e+09	446882
1.43257e+06	1.55696e+06	6.8103e+06	479265	446882	3.35838e+09

The elasticity matrix obtained from the homogenization process allows for the calculation of various material properties, including the elastic modulus (Equation 1,Equation 2), shear modulus (Equation 3) and Poisson's ratio(Equation 4).

$$S_{ij} = {C_{ij}}^{-1}$$

Equation 1. Compliance matrix calculation

$$E_x = \frac{1}{S_{11}}$$

Equation 2. Effective Elastic Modulus in the x-direction

$$G_{ij} = \frac{1}{S_{ij}}$$

Equation 3. Shear moduli

$$\nu_{ij} = \frac{S_{ij}}{-S_{ii}}$$

Equation 4. Poisson's Ratio

The following Python code seen in Figure 4.6 was used to perform these calculations:

```
import numpy as np
C_image_matrix_values = [
    [1.18978e+10, 5.91482e+09, 5.91474e+09, 6.42017e+06, 1.44192e+06, 1.43257e+06],
    [5.91482e+09, 1.18978e+10, 5.91472e+09, 1.14988e+06, 6.62046e+06, 1.55696e+06],
    [5.91474e+09, 5.91472e+09, 1.18974e+10, 1.35330e+06, 1.40950e+06, 6.81030e+06],
    [6.42017e+06, 1.14988e+06, 1.35330e+06, 3.35847e+09, 4.67168e+05, 4.79265e+05],
    [1.44192e+06, 6.62046e+06, 1.40950e+06, 4.67168e+05, 3.35842e+09, 4.46882e+05],
    [1.43257e+06, 1.55696e+06, 6.81030e+06, 4.79265e+05, 4.46882e+05, 3.35838e+09]
]
C_image_matrix = np.array(C_image_matrix_values)
S_image_matrix = np.linalg.inv(C_image_matrix)
E_x_image_matrix = 1 / S_image_matrix[0, 0]
E_y_image_matrix = 1 / S_image_matrix[1, 1]
E_z_image_matrix = 1 / S_image_matrix[2, 2]
G_xy_image_matrix = 1 / S_image_matrix[3, 3]
G_yz_image_matrix = 1 / S_image_matrix[4, 4]
G_zx_image_matrix = 1 / S_image_matrix[5, 5]
nu_xy_image_matrix = -S_image_matrix[0, 1] / S_image_matrix[0, 0]
nu_yz_image_matrix = -S_image_matrix[1, 2] / S_image_matrix[1, 1]
nu_zx_image_matrix = -S_image_matrix[2, 0] / S_image_matrix[2, 2]
E_mean_image_matrix = (E_x_image_matrix + E_y_image_matrix + E_z_image_matrix) / 3
nu_mean_image_matrix = (nu_xy_image_matrix + nu_yz_image_matrix + nu_zx_image_matrix) /
3
K_image_matrix = E_mean_image_matrix / (3 * (1 - 2 * nu_mean_image_matrix))
results_image_matrix = {
    "E_x": E_x_image_matrix,
    "E_y": E_y_image_matrix,
    "E_z": E_z_image_matrix,
    "G_xy": G_xy_image_matrix,
    "G_yz": G_yz_image_matrix,
    "G_zx": G_zx_image_matrix,
    "nu_xy": nu_xy_image_matrix,
    "nu_yz": nu_yz_image_matrix,
    "nu_zx": nu_zx_image_matrix,
    "K": K_image_matrix
}
```

Figure 4.6 Python code to find material properties

From this calculation, the following material properties were obtained:

Elastic Moduli:

Ex≈7.97×109Ex≈7.97×109 Pa (or 7.97 GPa)

Ey≈7.97×109Ey≈7.97×109 Pa (or 7.97 GPa)

Ez≈7.97×109Ez≈7.97×109 Pa (or 7.97 GPa)

Elastic Modulus (E): The calculated elastic moduli are significantly lower than the real value for Ti6Al4V (7.97 GPa vs. 113.8 GPa).

The homogenization results of the diamond lattice:

Degree of Freedom (DoF) Count: The analysis involved 2,209,191 degrees of freedom, indicating the complexity and detail of the model.

Element Count: A total of 455,444 elements were used in the finite element mesh, providing a refined representation of the lattice structure.

Node Count: The model comprised 736,397 nodes, which are the points at which the elements are connected.

Relative Density: The relative density of the gyroid lattice was found to be 0.1997, reflecting the proportion of solid material within the lattice structure.

Zener Ratio: The Zener ratio was calculated as 1.1227, indicating the degree of anisotropy in the elastic properties of the lattice.

The elasticity matrix of diamond lattice is shown in Table 4.4. The same calculations shown in Figure 4.6 has been applied to find material properties.

Table 4.4 Elasticity matrix of diamond lattice

1.5719e+09	**7.43444e+08**	**7.43048e+08**	**-2.23613e+06**	**600920**	**1.04635e+08**
7.43444e+08	1.65863e+09	7.87087e+08	3.11624e+07	-2.98059e+07	2.56336e+07
7.43048e+08	7.87087e+08	1.66923e+09	6.43322e+06	-3.58017e+07	8.66232e+07
-2.23613e+06	3.11624e+07	6.43322e+06	7.81431e+08	-3.19316e+07	-2.74265e+07
600920	-2.98059e+07	-3.58017e+07	-3.19316e+07	8.11593e+08	-2.95751e+07
1.04635e+08	2.56336e+07	8.66232e+07	-2.74265e+07	-2.95751e+07	7.65161e+08

The results are,

Elastic Moduli:

Ex≈1.1×109Ex≈1.1×109 Pa

Ey≈1.1×109Ey≈1.1×109 Pa

Ez≈1.1×109Ez≈1.1×109 Pa

Elastic Moduli: The provided matrix has significantly lower elastic moduli compared to Ti6Al4V and Gyroid.

Table 4.5 FEA results of lattice structures

Sample	Maximum and minimum Von mises points and values	Colormap
Gyroid		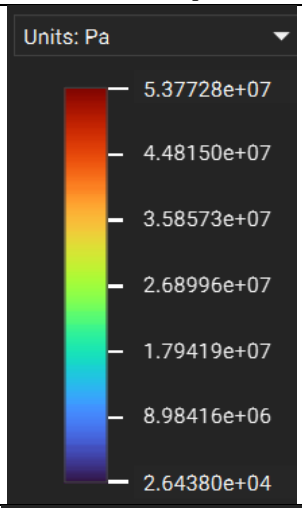
Diamond		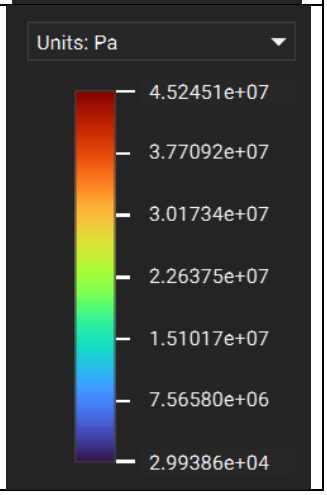

Table 4.5 shows the final results of lattices under given load conditions. According to the analysis made the results has been shown in Table 4.6.

Table 4.6 The von mises results of lattice samples and its comparison with Ti64 yield strength

Lattice Type	**Maximum Von Mises**	**The yield stregth of Titanium**	**Safety Factor**
Diamond	4.52451e+07 Pa	8.8e+08 Pa	19.44
Gyroid	5.37728e+07 Pa		16.36

4.3.1 Interpretation of FEA results of gyroid

Safety Factor Calculation:

Safety Factor=Yield Strength/Maximum von Mises Stress=8.8e+8 Pa/5.37728e+7 Pa≈16.36

A safety factor of 16.36 indicates that the maximum stress experienced by the material is well below its yield strength, implying a very safe design.

Stress Distribution: The maximum von Mises stress of 53.77 MPa is significantly lower than the yield strength of Ti64, ensuring that the material will not undergo plastic deformation.

The minimum von Mises stress of 0.0264 MPa indicates regions of negligible stress, which are not of concern.

Critical Regions: There are no regions where the von Mises stress exceeds the yield strength. This ensures that the material should not experience any plastic deformation under the given loading conditions. However, high-stress areas should be inspected for

potential stress concentration points. Given the significant safety factor, these are unlikely to pose a problem.

4.3.2 Interpretation of FEA results of diamond

Safety Factor Calculation:

Safety Factor=Yield Strength/Maximum von Mises Stress=8.8e+8 Pa/4.52451e+7 Pa≈1 9.44

A safety factor of 19.44 indicates that the maximum stress experienced by the material is well below its yield strength, implying a very safe design.

Stress Distribution: The maximum von Mises stress of 45.25 MPa is significantly lower than the yield strength of Ti64.

The stress distribution suggests that the material is under low stress relative to its capacity, which indicates a robust design with minimal risk of yielding.

Critical Regions: There are no regions where the von Mises stress exceeds the yield strength, ensuring that the material will not undergo plastic deformation under the given loading conditions.

4.4 Biomimetic Integration

The integration has been applied to lattice shell located outer surface of acetabular cup. The porosity value (79.8%) and the geometry has been give in Figure 4.7.

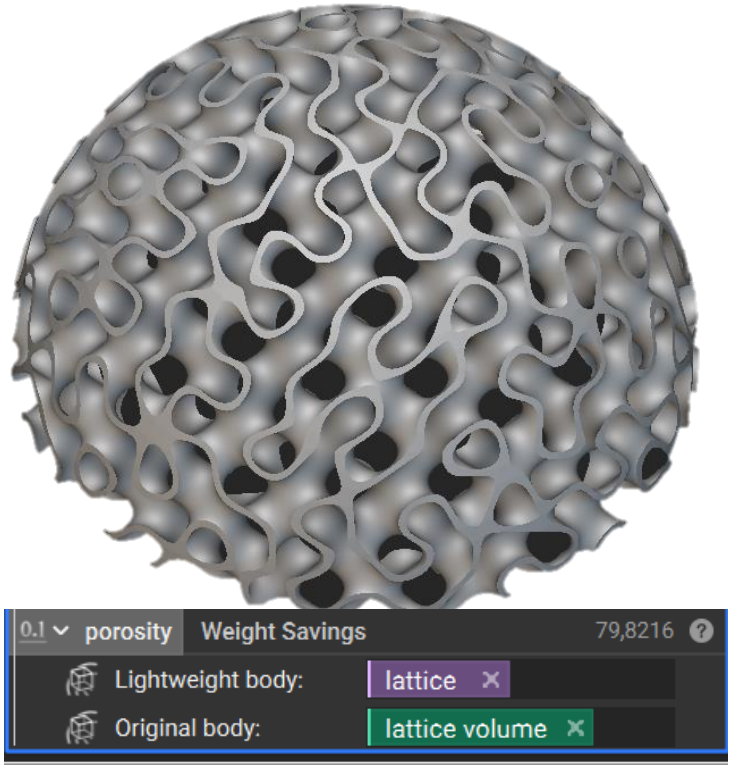

Figure 4.7 Biomimetic design and porosity value obtained

4.5 Topology Optimization of Stem Component

The boundary conditions for the stem and femur models were configured as shown in the Figure 4.8, and the finite element (FE) model was subsequently created.

Figure 4.8 Boundary conditions of stem FE model

The initial analysis was performed under these boundary conditions, and the results are presented in the Figure 4.9. The isolated FEA results for the stem geometry are also illustrated in the Figure 4.10.

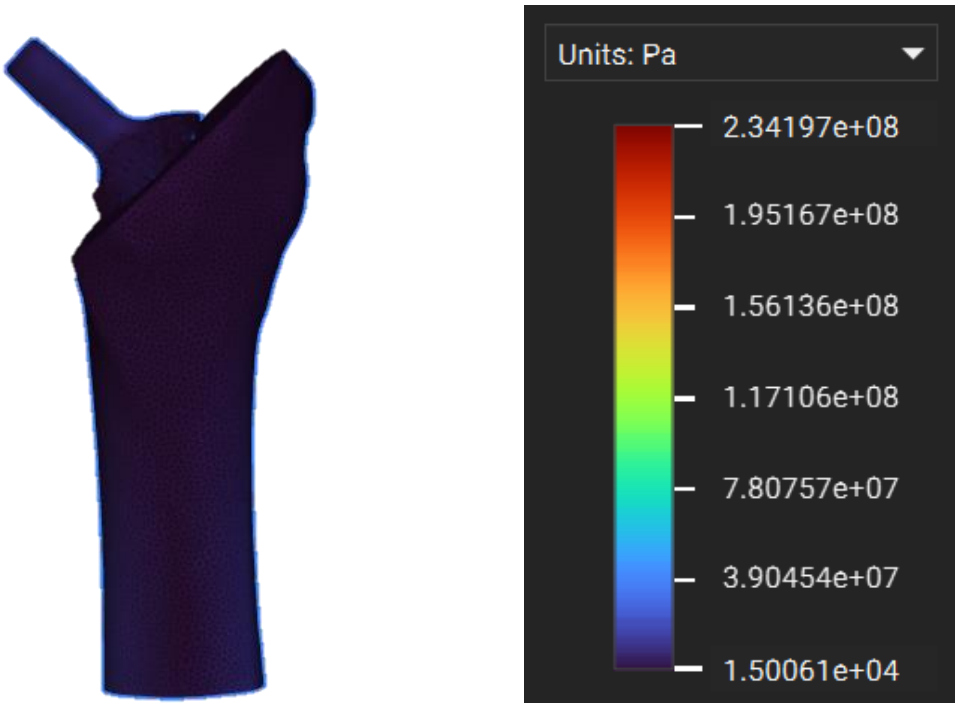

Figure 4.9 Stem-femur FE model FEA result

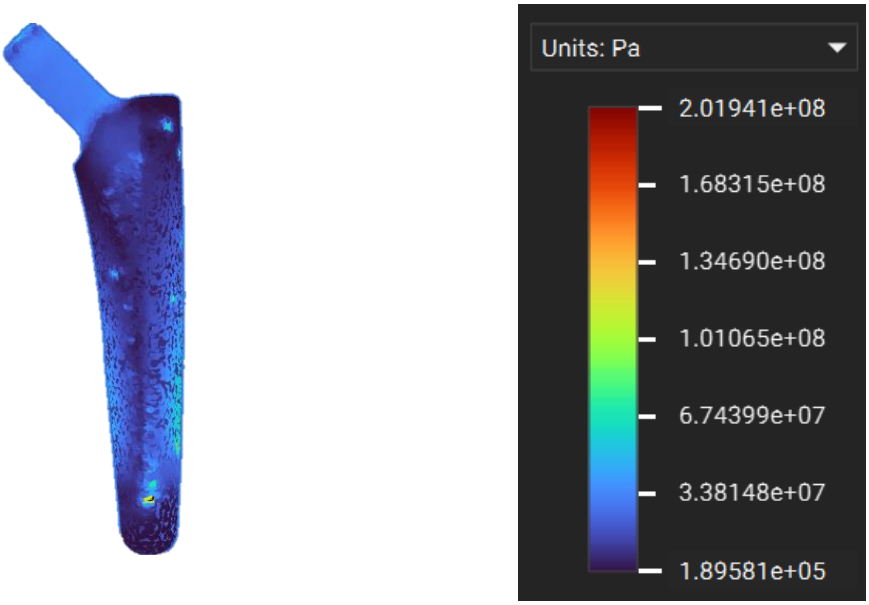

Figure 4.10 Isolated stem FEA result

4.5.1 Interpretation of results of bulk stem

Safety Factor Calculation: The safety factor (SF) is calculated by dividing the material's yield strength by the maximum von Mises stress observed:

Safety Factor=Yield Strength/Maximum von Mises Stress=8.8e+8 Pa/2.011941e+8 Pa≈ 4.37

A safety factor of 4.37 indicates that the maximum stress experienced by the material is well below its yield strength, implying a safe design with a considerable margin before yielding occurs.

Stress Distribution: The maximum von Mises stress of 201.19 MPa is significantly lower than the yield strength of Ti64, ensuring that the material will not undergo plastic deformation under the given loading conditions.

The stress distribution is favorable, indicating that the material is not close to its failure limits.

Critical Regions: No regions where the von Mises stress exceeds the yield strength, confirming the absence of plastic deformation under the applied loading.

The geometry obtained after the data-driven design steps is illustrated in the Figure 4.11.

Figure 4.11 Data driven design of stem

In the FEA conducted based on the FE model shown in the Figure 4.12, the topologically optimized stem demonstrated the performance illustrated in the Figure 4.13.

Figure 4.12 Optimized stem - femur FE model

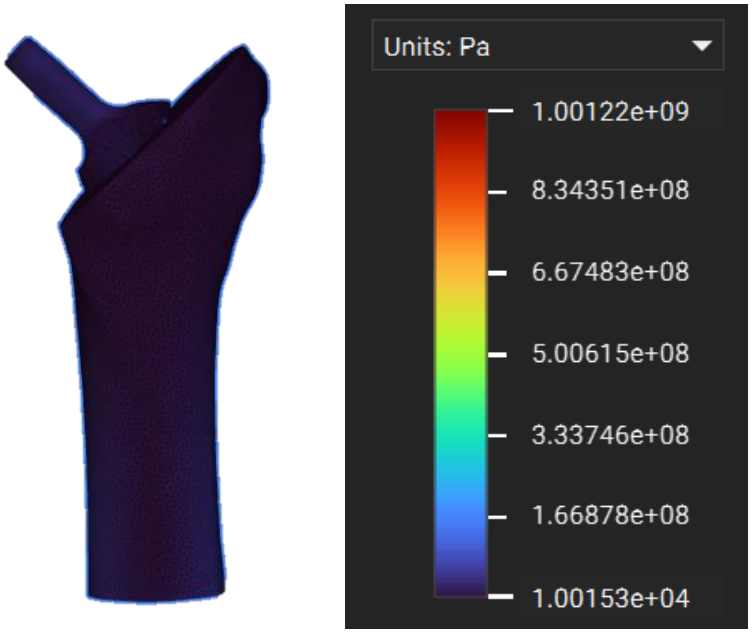

Figure 4.13 Optimized stem static analyis result

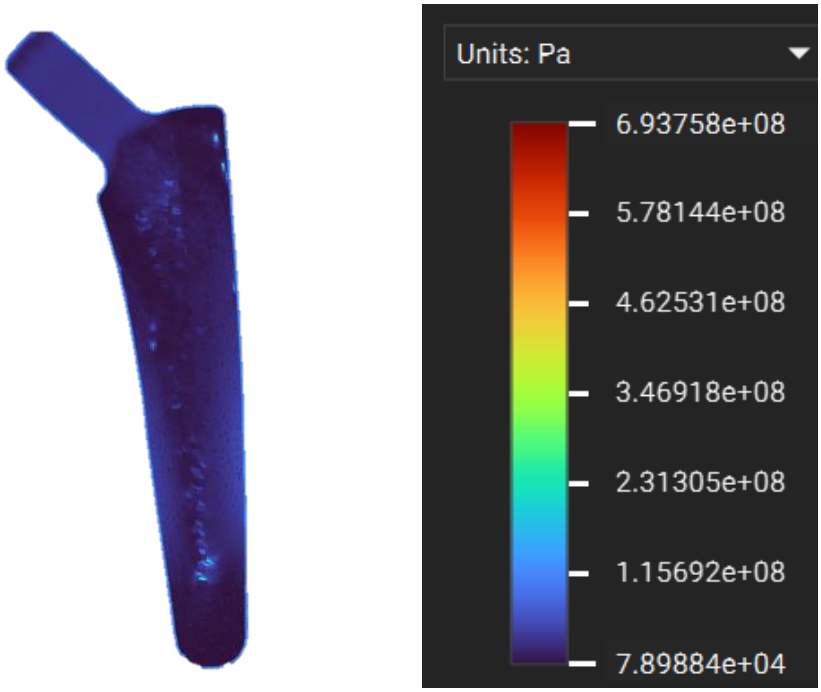

Figure 4.14 Isolated optimized stem FEA results

Table 4.7 According to stem types the comparison of the safety factors

Stem type	**Maximum Von Mises**	**The yield stregth of Titanium**	**Safety Factor**
Bulk	2.011941e+8 Pa	8.8e+08 Pa	4.37
Topologically optimized	6.93758e+08 Pa		≈1

The isolated results shown in the figure indicate that the maximum stress on the optimized stem is 6.93758e+08 Pa. Based on this, the following analysis can be performed:

Safety Factor=Yield Strength/Maximum von Mises Stress=8.8e+8 Pa/6.93758e+8 Pa≈1.

A safety factor of 1.27 indicates that the maximum stress experienced by the material is close to its yield strength. This implies that the design is relatively safe but has limited margin before yielding occurs.

Stress Distribution: The maximum von Mises stress of 693.76 MPa is close to the yield strength of Ti64. This indicates that the material is approaching its plastic deformation limit under the applied loading conditions.

Critical Regions: Areas with stress levels near the maximum von Mises stress should be carefully examined for potential stress concentration points. Any regions with stress exceeding the yield strength may experience plastic deformation.

The comparison between bulk and topologically optimized stem according to maximum von mises values and safety factor has been given in Table 4.7

4.6 In Vitro

4.6.1 Indirect cytotoxicity test results

The morphological examination results after the addition of the extraction fluid to the samples (Figure 4.15 and Figure 4.16), the viability analysis (Figure 4.17), and the cytotoxicity evaluation results are presented below.

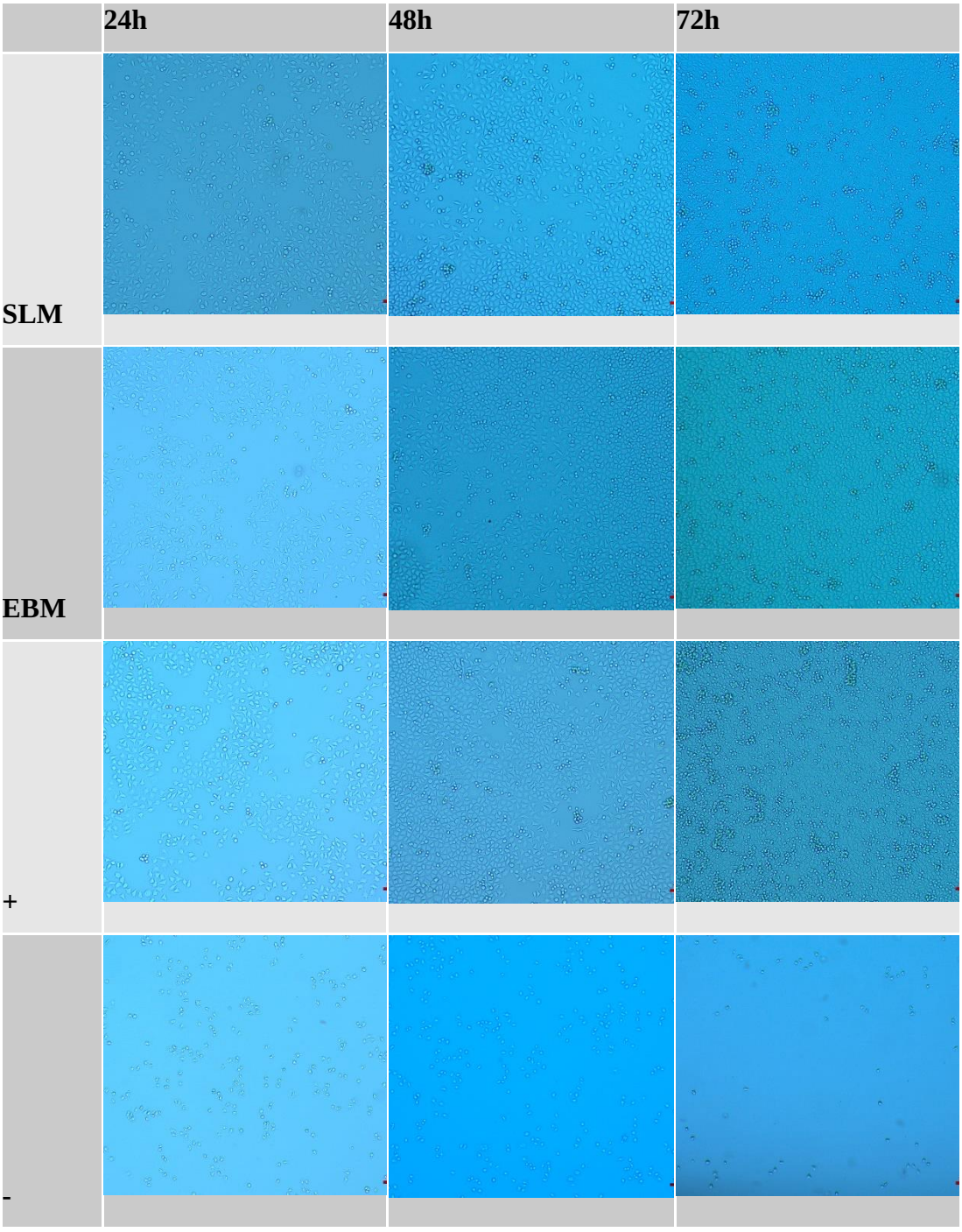

Figure 4.15 Changes in cell layer confluency at 24, 48, and 72 hours after the addition of extraction fluid for SLM, EBM, positive and negative samples (10x magnification)

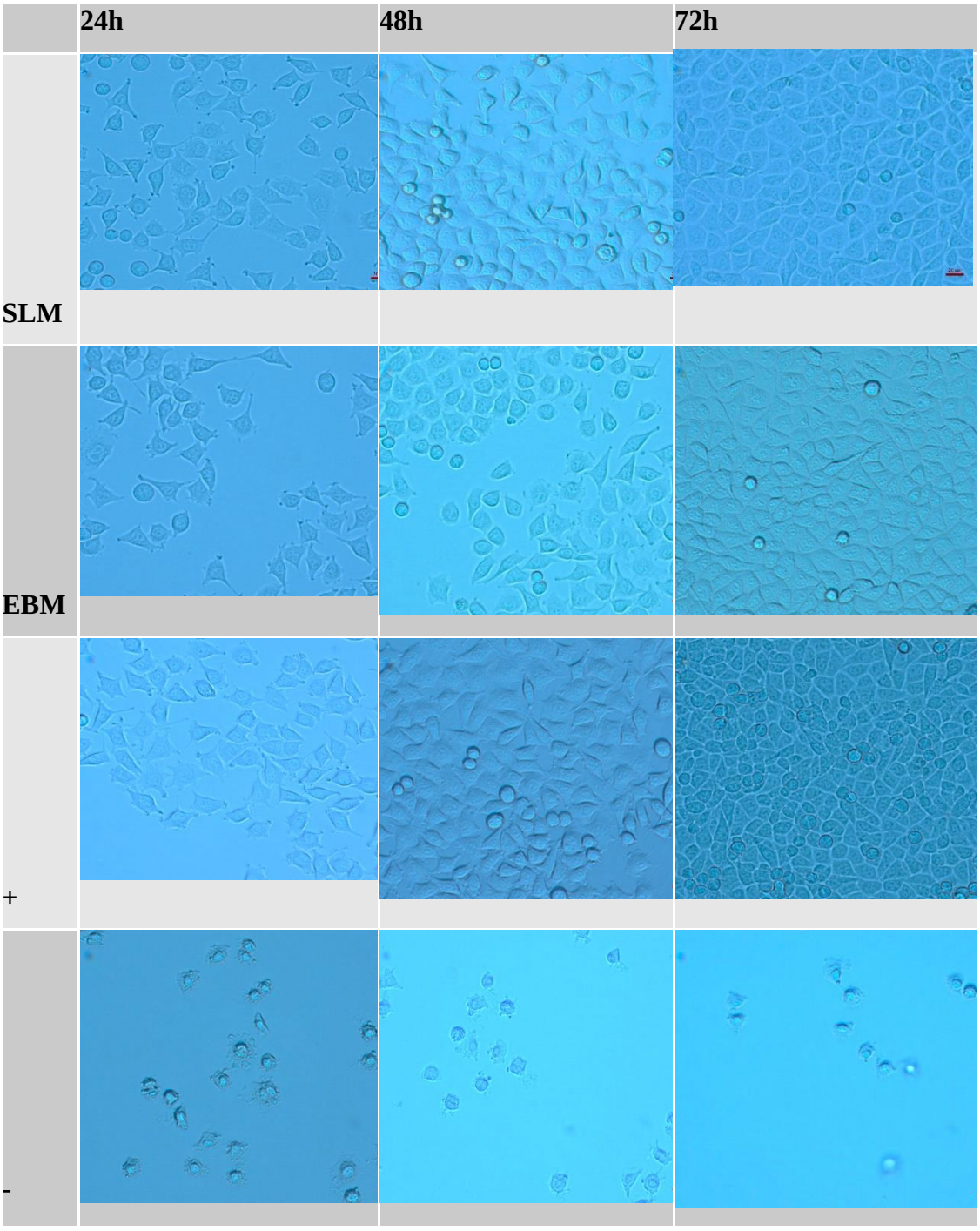

Figure 4.16 Changes in cell morphology at 24, 48, and 72 hours for experimental groups after the addition of extraction fluid (40x magnification)

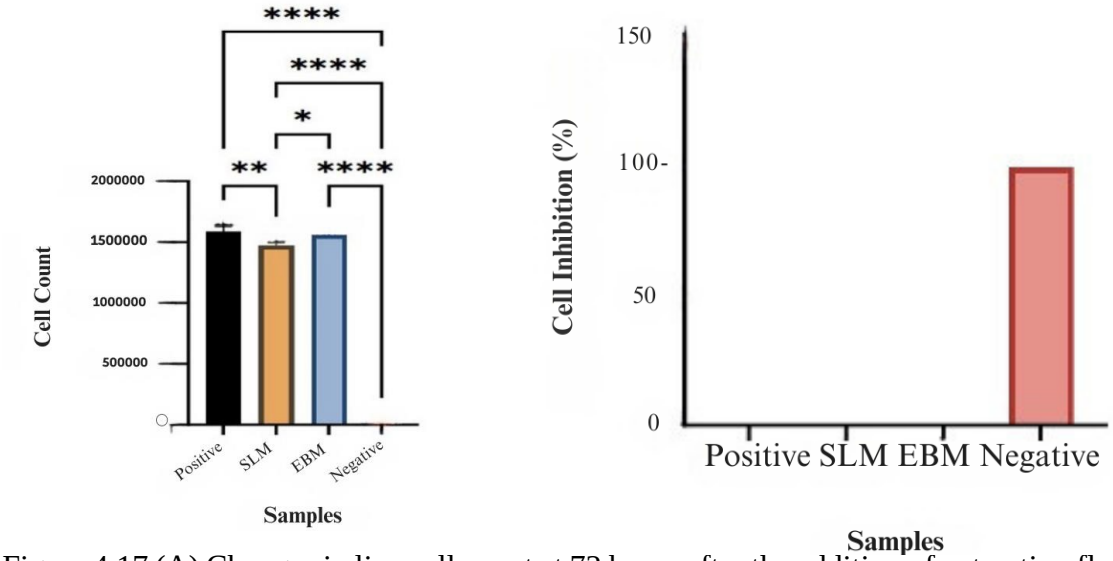

Figure 4.17 (A) Changes in live cell count at 72 hours after the addition of extraction fluid for experimental groups; results are normalized relative to the negative control group. (B)% inhibition of cell growth; results are presented relative to the positive control group. (n=3 *p<0.0101 **p<0.0020 ****p<0.0001)

Based on the microscopic examination and cell counting results, the outcomes of the experimental groups according to the "cytotoxicity test evaluation criteria" scoring table are presented in

Table 4.8.

Table 4.8 Results of cytotoxicity test evaluation criteria

	Group	Note		Group	Note
Cell layer (Confluency)	SLM	1	Cell in its morphology change	SLM	1
	EBM	1		EBM	1
Amount of dead cells (Floating cells)	SLM	1	Cell growth inhibition	SLM	0
	EBM	1		EBM	0

Based on these results, the cytotoxicity response index and cytotoxicity evaluation results for metal implant materials are presented in Table 4.9. According to these results, SLM and EBM are not cytotoxic.

Table 4.9 Cytotoxicity evaluation results for metal implant samples produced by SLM and EBM methods

Group	Cytotoxicity index	Material is cytotoxic
SLM	1	No
EBM	1	No

4.6.2 Cell viability analysis and osteogenic differentiation

The results of the cell viability analysis applied to the samples in vitro on days 3, 7, and 14 of the culture are shown in Figure 4.18.

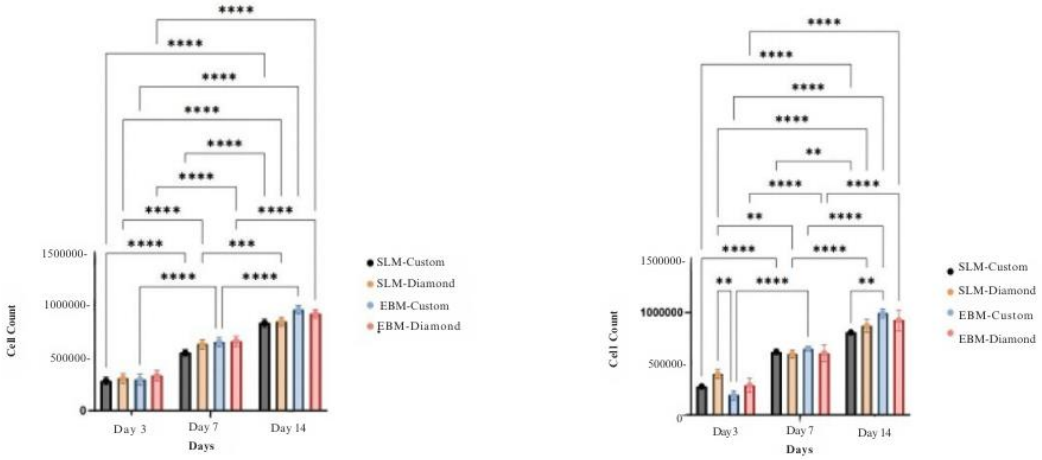

Figure 4.18 The number of live cells observed during the 14-day culture period after direct seeding (A) and seeding within fibrin gel (B) on metal samples produced by SLM and EBM methods with different geometries. (n=3 **p<0.0013 ***p<0.0004 ****p<0.0001)

4.6.3 Surface characterization of implants with SEM analysis

SEM analysis was performed on the samples before cell seeding to characterize the surface and pattern structures. The results are presented in Figure 4.19.

Sample		Gyroid	Diamond	Custom
EBM	50X	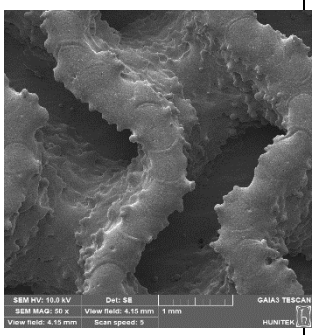	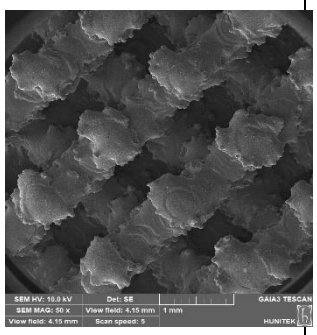	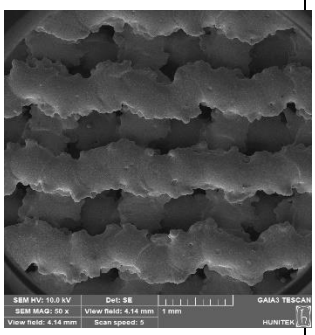
	100 X	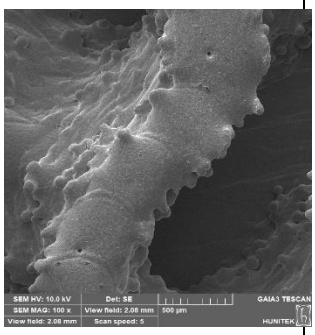	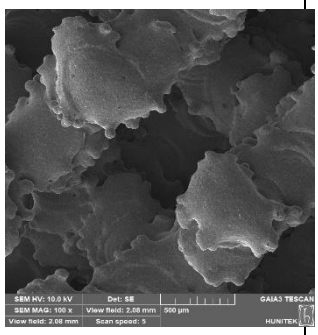	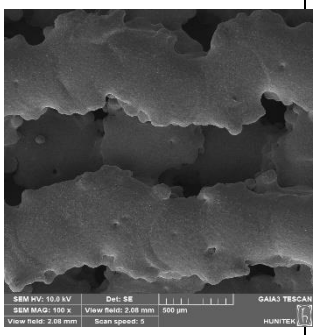
SLM	50X	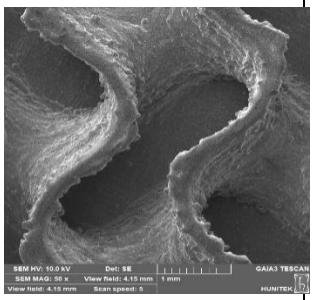	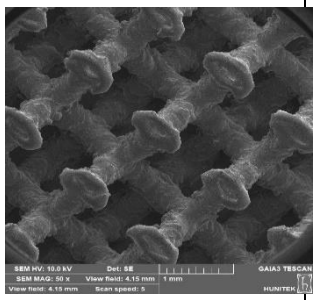	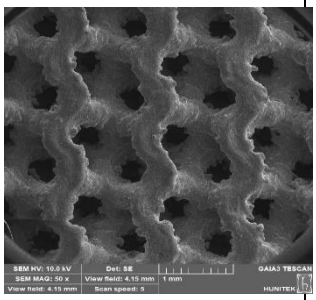
	100 X	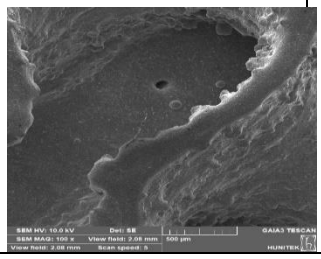	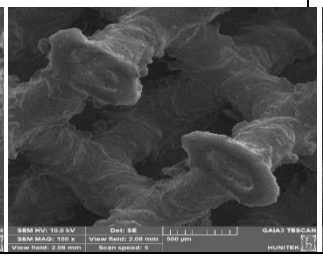	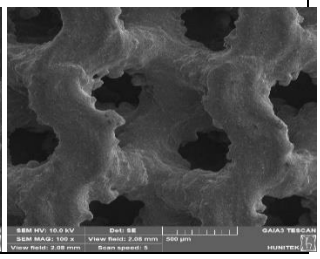

Figure 4.19 Surface examination images of metal samples Gyroid, Diamond and Custom lattices produced with SLM and EBM before cell seeding

The SEM images obtained from the analysis performed on days 7 and 14 after cell seeding are presented in Figure 4.20.

SEM images (Day 7)			
Sample	**Gyroid**	**Diamond**	**Custom**
EBM	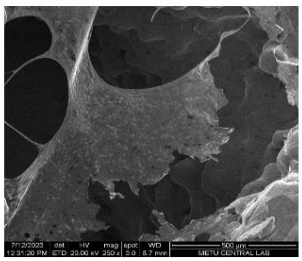	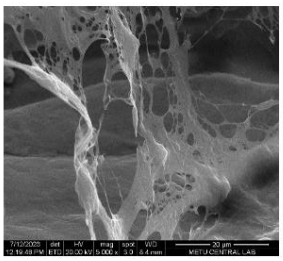	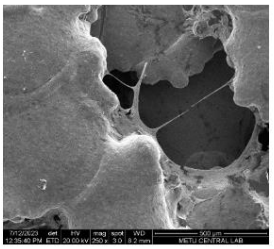
	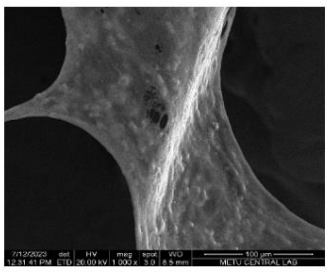	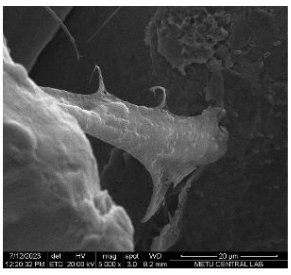	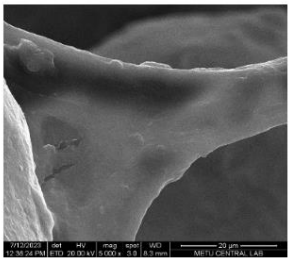
	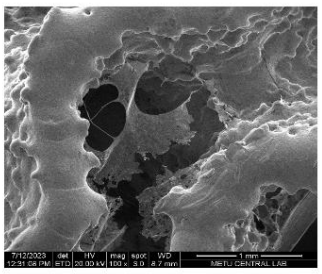	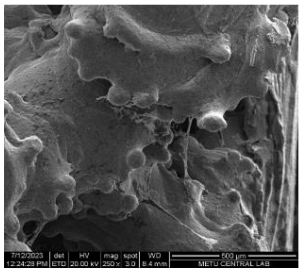	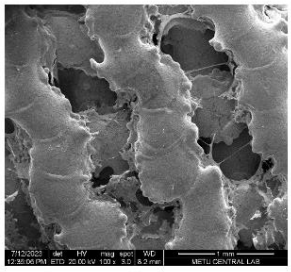

SEM Images Day 7			
Sample	**Gyroid**	**Diamond**	**Custom**
SLM	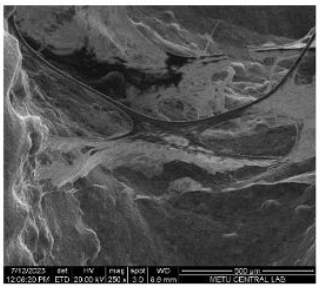	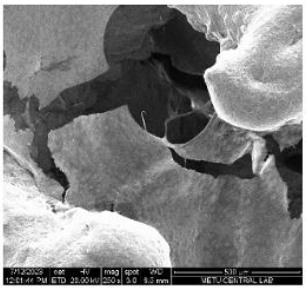	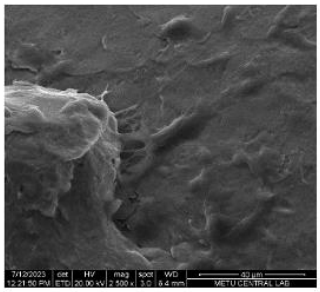
	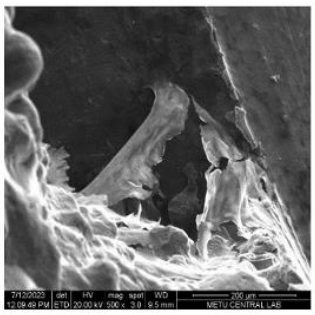	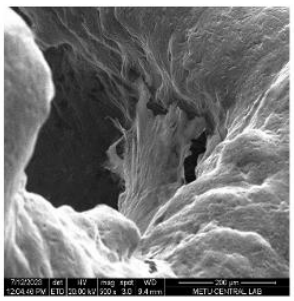	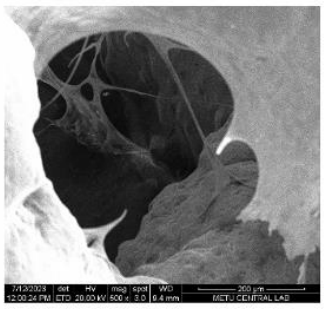
	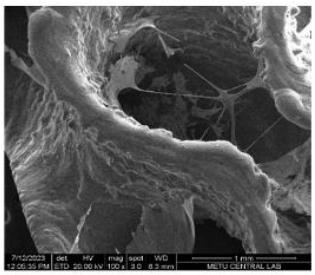	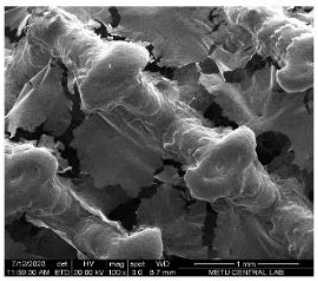	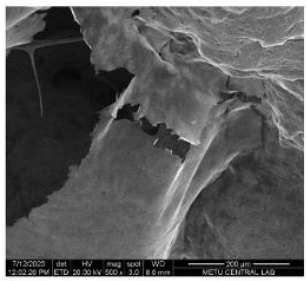

SEM images (Day 14)			
Sample	**Gyroid**	**Diamond**	**Custom**
EBM	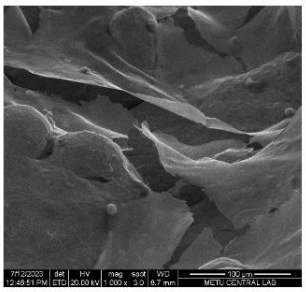	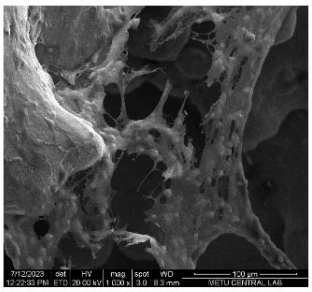	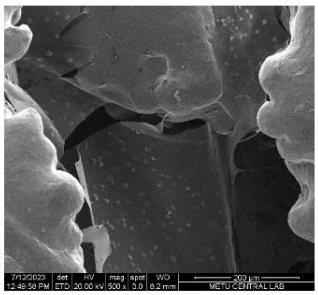
	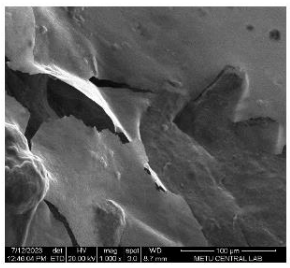	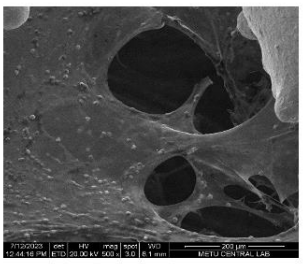	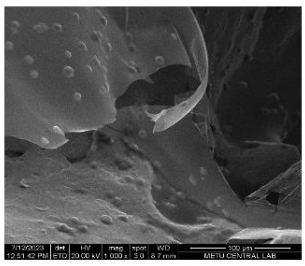
	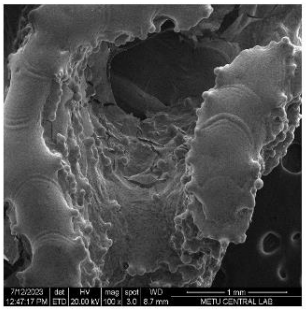	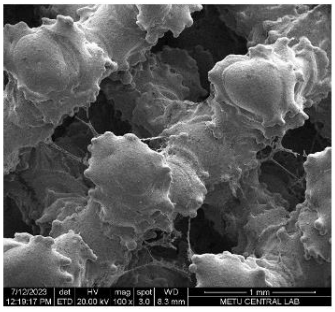	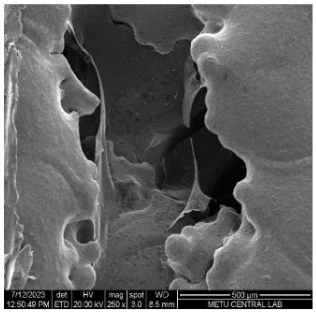

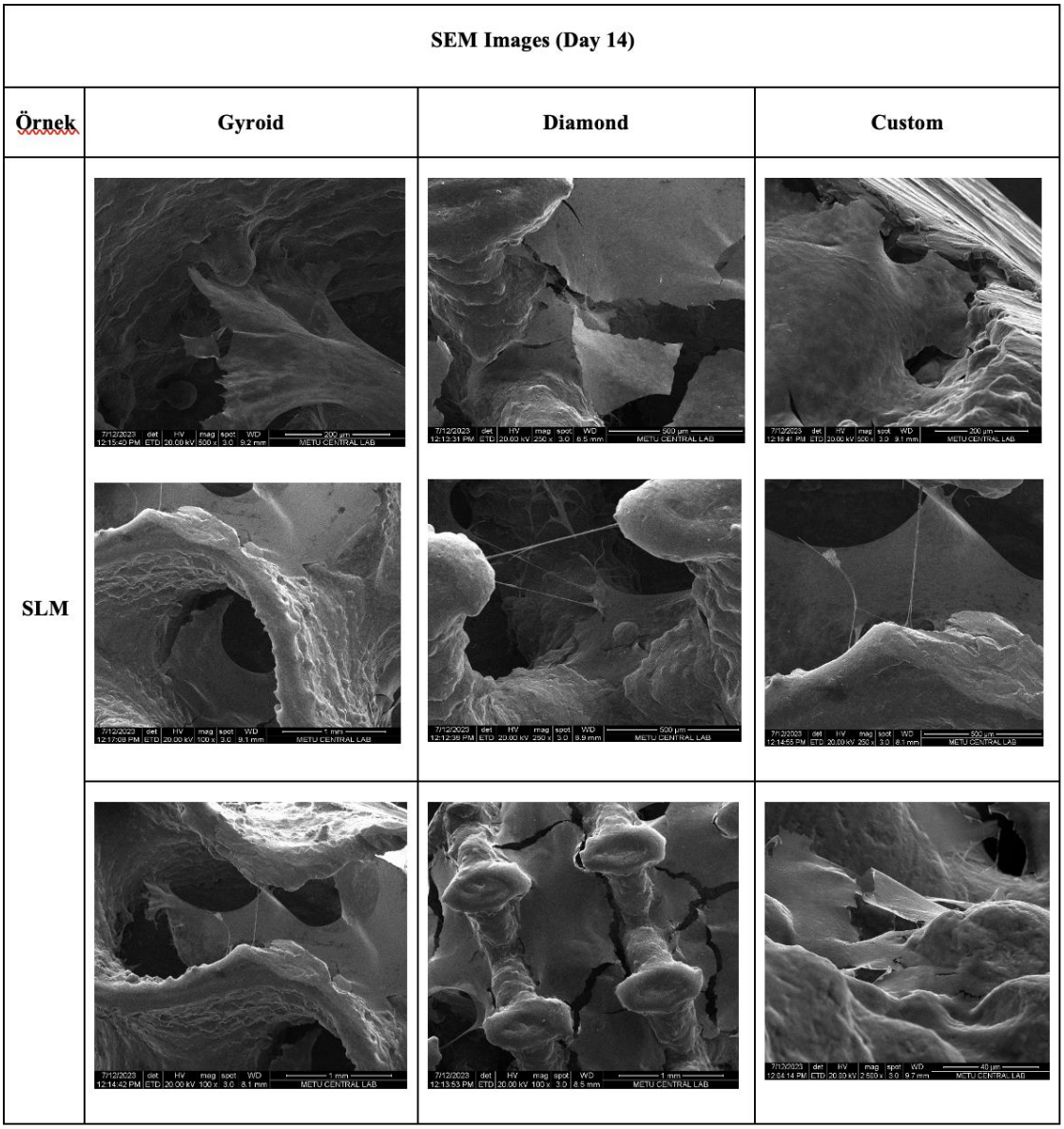

Figure 4.20 SEM images of cells on metal samples produced by EBM and SLM methods on days 7 and 14 of the culture

4.6.4 Visualization of cell distribution on metal implants using fluorescence microscopy

The nuclei of MC3T3 cells seeded onto the samples were stained with DAPI and imaged using fluorescence microscopy. The obtained images are presented in Figure 4.21.

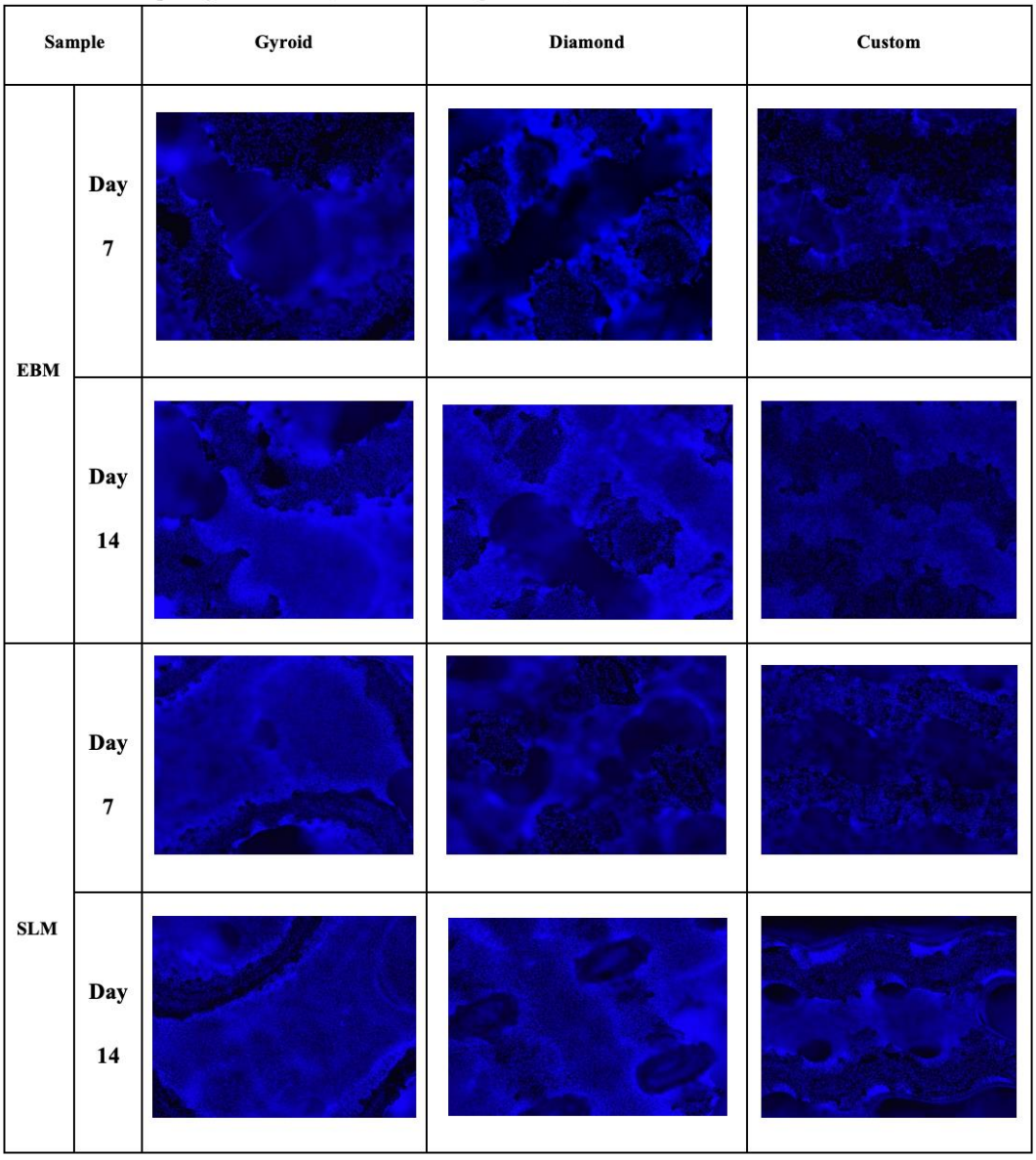

Figure 4.21 Homogeneous distribution of cells on metallic samples produced by EBM and SLM methods observed under a fluorescent microscope after staining the cell nuclei with DAPI (5x magnification)

4.6.5 Confocal Microscopy Images of Samples

Immunofluorescent labeling was used to examine osteopontin expression in cells seeded on metal implant samples on days 7 and 14 of the culture. Osteopontin is a bone-specific marker, and its expression was analyzed to investigate the effect of structural properties on the differentiation of preosteoblast cells into osteoblasts. The obtained images are presented in Figure 4.22.

Sample	Day 7	Day 14
EBM-GYROID 5X	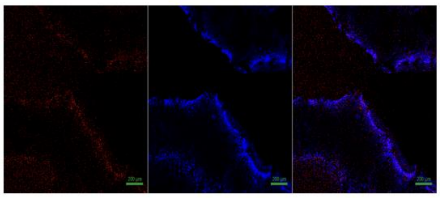	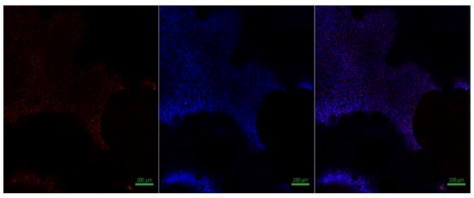
EBM-DIAMOND 5X	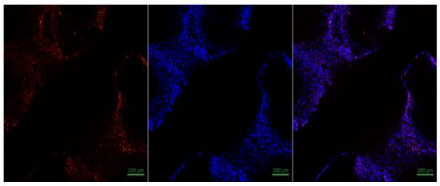	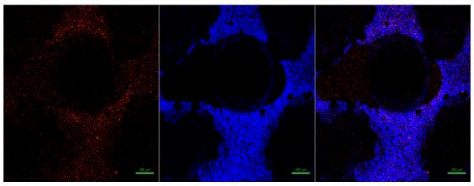
EBM-CUSTOM 5X	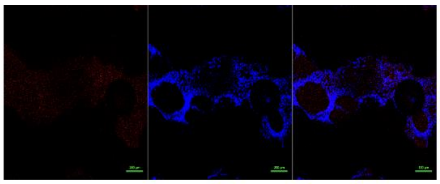	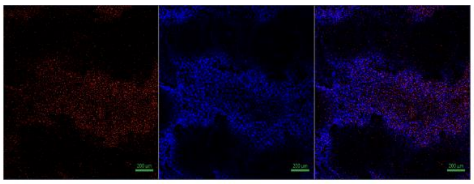

Samples	Day 7	Day 14
EBM-GYROID 20X	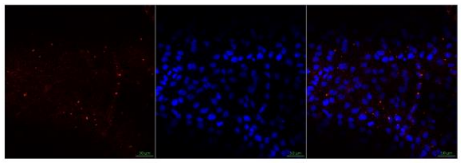	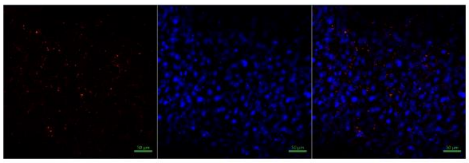
EBM-DIAMOND 20X	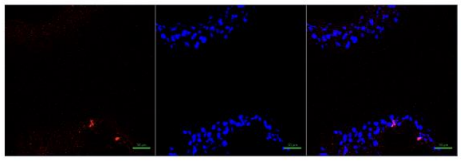	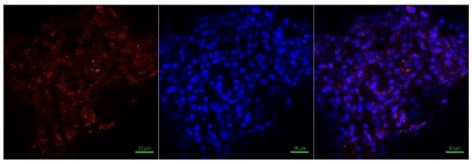
EBM-CUSTOM 20X	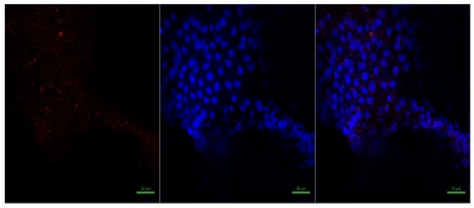	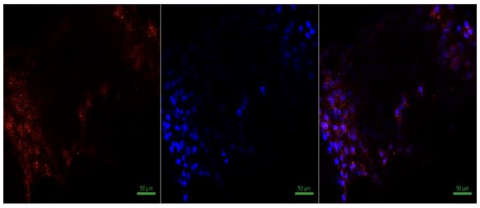

Samples	Day 7	Day 14
SLM-GYROID 5X	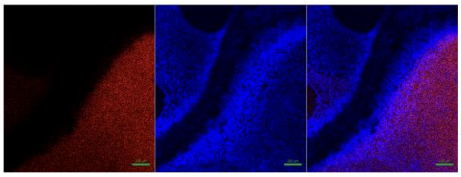	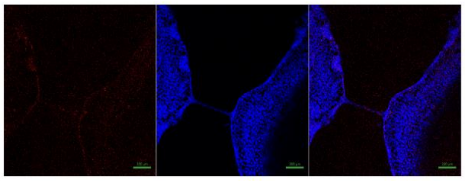
SLM-DIAMOND 5X	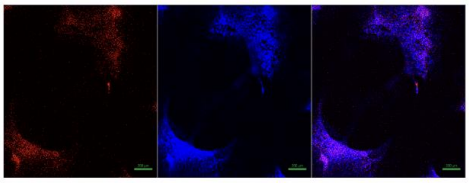	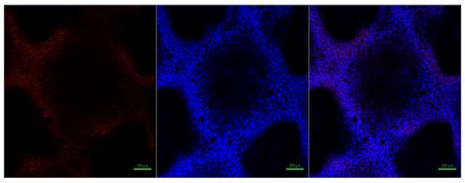
SLM-CUSTOM 5X	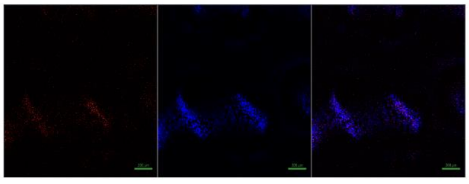	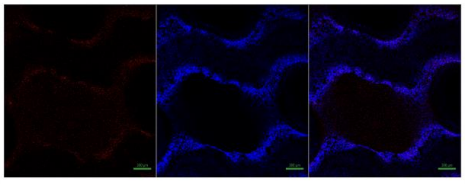

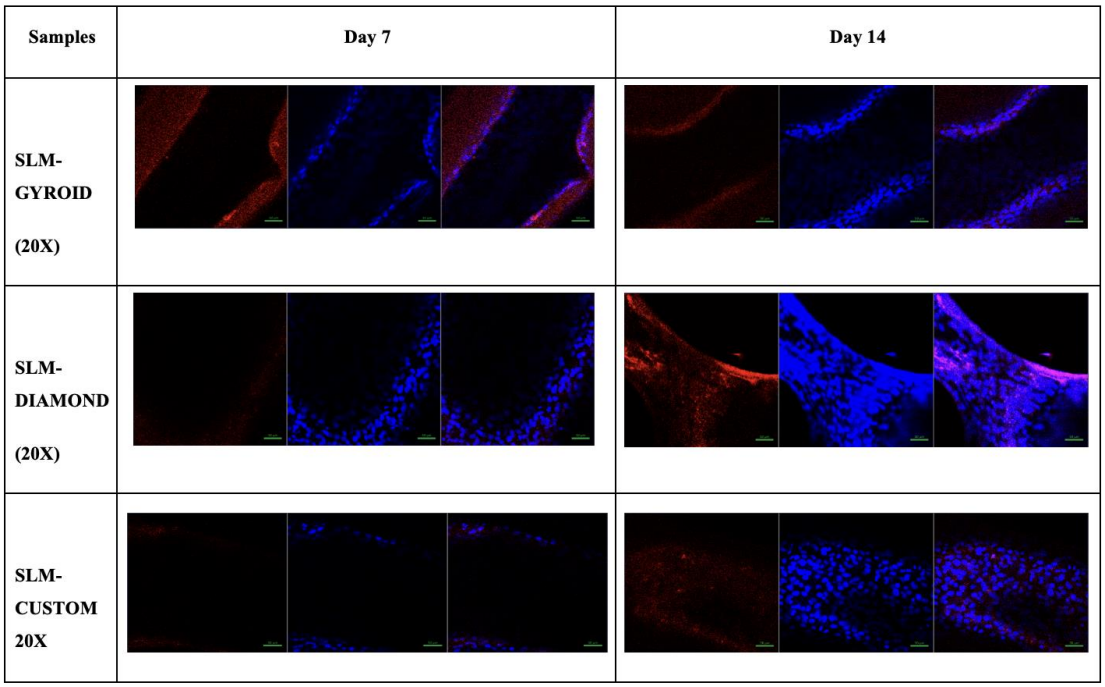

Figure 4.22 Osteopontin/DAPI fluorescent staining images of cell cultures on metal samples performed on days 7 and 14

4.6.6 Staining intensity values

The staining intensity in the context of confocal microscopy images refers to the amount of fluorescent signal emitted from a sample stained with fluorescent dyes or antibodies. The staining intensity values for Osteopontin/DAPI in the 5x magnification confocal images are shown in Figure 4.23. The values are normalized to Osteopontin levels.

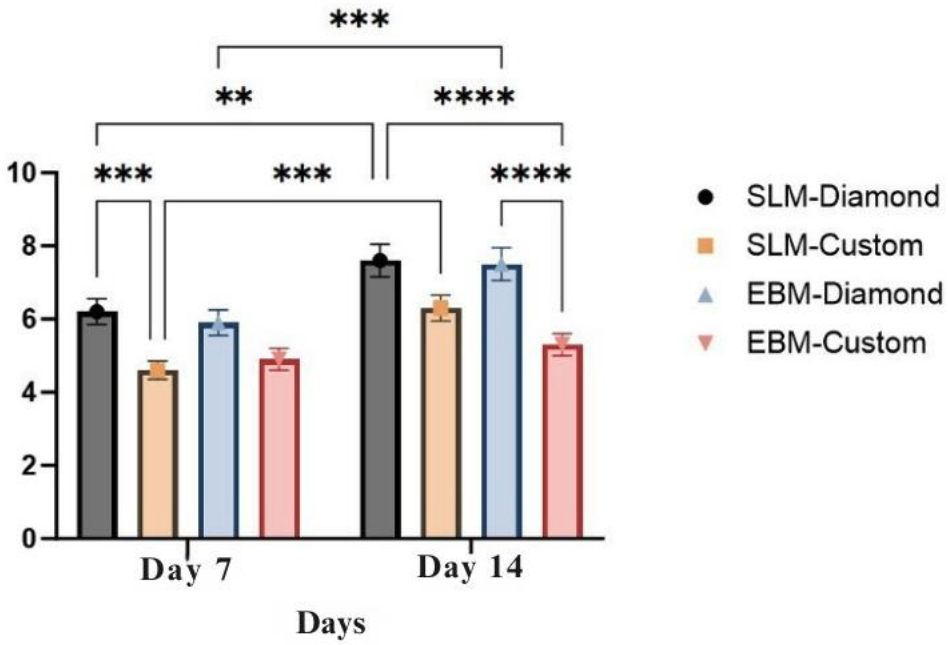

Figure 4.23 Osteopontin/DAPI fluorescent staining intensity values from confocal microscope images of EBM and SLM implants (5x magnification) (n=3 **p<0.0037 ***p<0.0005 ****p<<0.0001)

4.6.7 Alkaline phosphatase activity assay results

To quantitatively evaluate osteogenic differentiation, ALP activity was assessed in the samples. ALP activity is a common method used to detect osteogenic differentiation (Reible et al. 2017, Sun et al. 2010). The amount of p-nitrophenol phosphate generated by samples per minute was examined under a plate reader as the absorbance of p-nitrophenol at 405 nm. The graph of readings taken from each group in nmol/min/well/cell number is shown in Figure 4.24.

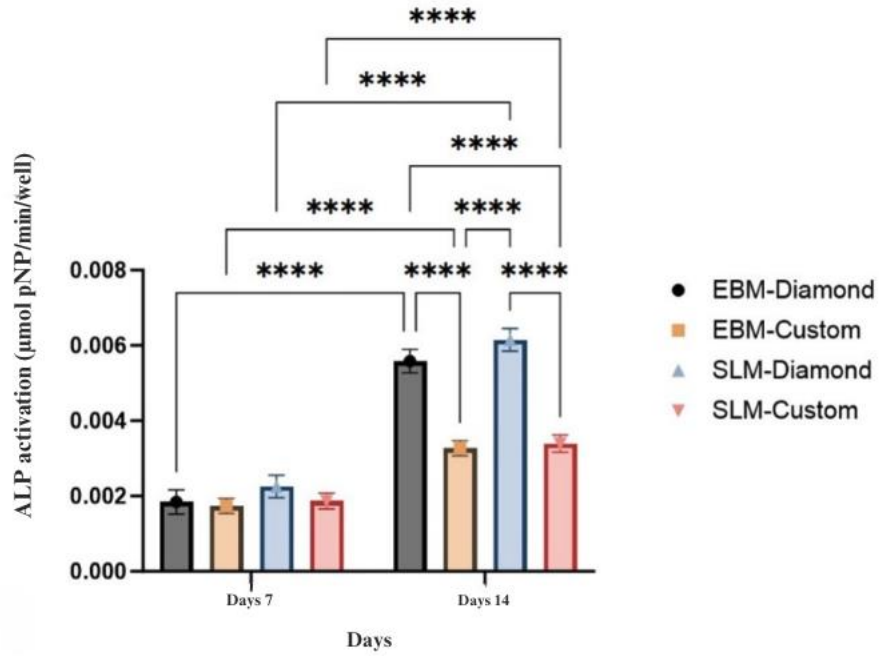

Figure 4.24 ALP analysis results of the samples. ALP enzyme activity reflects the amount of p-NP formed per minute (n=3 ****p<<0.0001)

4.6.8 Discussion of in-vitro results

As observed in the SEM images post-experiment, cell clusters exhibited a tendency to cover each pattern of both groups in layers/sheets. When examining the homogeneous distribution of cells (for day 14 samples), it was found that Diamond samples had more uniform distributions compared to the other groups.

Cell proliferation refers to the process where cells divide and multiply, leading to an increase in cell numbers. Differentiation, on the other hand, is the process by which cells specialize and acquire specific functions. In most cases, when cells are actively proliferating, their potential for differentiation may be lower.

Upon analyzing the ALP results and confocal microscopy images, the following ranking was observed: Diamond > Gyroid

When considering all the results together, it was concluded that the differences in pattern and production technique did not result in a statistically significant difference in cell proliferation. However, in terms of inducing cell differentiation, the groups were ranked as “diamond” followed by “gyroid.”

4.7 Ongoing and Future Work

The subject of this thesis is ongoing as work packages under a TÜBİTAK project at Btech company (Project No: 3230398). The product to be obtained as a result of the project will be a size of a hip implant set for dogs. The product is expected to be commercialized in 2025.

5. CONCLUSION

This thesis has successfully developed a comprehensive total hip prosthesis system with a trabecular surface specifically designed to enhance osseointegration for canine patients. Through meticulous design and innovative application of lattice structures, the study underscores the potential of biomimetic approaches in orthopedic implant development. The integration of structural tests using finite element analysis methods has validated the mechanical robustness of the designed implants, while in-vitro tests have confirmed the bioactivation properties of the materials used.

The findings of this research highlight significant mechanical and biological advantages, demonstrating that biomimetic design principles can markedly improve the effectiveness and functionality of total hip prostheses for dogs. The study also emphasizes the crucial role of additive manufacturing technologies, particularly powder bed fusion, in the fabrication of these advanced implants. This method allows for the precise creation of complex structures that mimic natural bone, thereby facilitating better osseointegration and overall implant performance.

In conclusion, this research has provided valuable insights into the development of orthopedic solutions that enhance the quality of life for canine patients. The successful implementation of advanced materials and innovative manufacturing techniques sets a promising precedent for future advancements in veterinary orthopedic implants. The mechanical and biological benefits observed in this study advocate for the continued exploration and application of biomimetic and additive manufacturing technologies in the field of veterinary orthopedics.

REFERENCES

Allan, G., & Davies, S. (2018). Radiographic signs of joint disease in dogs and cats. In *Textbook of Veterinary Diagnostic Radiology*.

Anderson, A. (2011). Treatment of hip dysplasia.

Andronescu, A. A., Kelly, L., & Kearney, M. T. (2015). Associations between early radiographic and computed tomographic measures and canine hip joint osteoarthritis at maturity. American Journal of Veterinary Research.

Ashby, M. F. (2006). The properties of foams and lattices. Philosophical Transactions of the Royal Society A: Mathematical, Physical and Engineering Sciences, 364(1838), 15-30.

Bar-Cohen, Y. (2011). Biomimetics: Nature-Based Innovation. CRC Press.

Belshaw, Z., & Yeates, J. (2018). Assessment of quality of life and chronic pain in dogs. The Veterinary Journal. Elsevier.

Bendsøe, M. P., & Sigmund, O. (2003). Topology Optimization: Theory, Methods, and Applications. Springer.

Bishop, C. M. (2006). Pattern Recognition and Machine Learning. Springer.

Brackett, D., Ashcroft, I., & Hague, R. (2011). Topology optimization for additive manufacturing. In Proceedings of the Solid Freeform Fabrication Symposium (pp. 348-362).

Cason, R. A. (2014). Effects of Osteoarthritis and Chronic Pain Management for Companion Animals.

Chen, Q., Wang, T., & Liu, J. (2022). Surface engineering of orthopedic implants: Recent advances and challenges. Journal of Biomedical Materials Research Part B: Applied Biomaterials, 110(6), 1265-1278.

Choy, S. Y., Sun, C. N., Leong, K. F., & Wei, J. (2019). Compressive properties of functionally graded lattice structures manufactured by selective laser melting. Materials & Design, 162, 394-404.

Cook, R. D., Malkus, D. S., Plesha, M. E., & Witt, R. J. (2012). Concepts and Applications of Finite Element Analysis. John Wiley & Sons.

Corr, S. (2007). Hip dysplasia in dogs: treatment options and decision making.

Davidson, J. R., & Kerwin, S. C. (2021). Management of traumatic hip injuries in dogs. Veterinary Orthopedic Journal.

Denny, H. R., Linnell, M., Maddox, T. W., & Comerford, E. J. (2018). Canine total hip replacement using a cementless threaded cup and stem: A review of 55 cases.

Deshpande, V., Fleck, N.A., & Ashby, M.F. (2001). Effective properties of the octet-truss lattice material. Journal of The Mechanics and Physics of Solids, 49, 1747-1769.

Fink, M., Wagner, T., & Hüfner, S. (2021). Advances in veterinary orthopedic surgery: A review of canine total hip replacement. Veterinary Surgery, 50(2), 215-224.

Gibson, I., Rosen, D. W., & Stucker, B. (2021). Additive manufacturing technologies. Springer.

Gibson, L. J., & Ashby, M. F. (1997). Cellular solids: Structure and properties. Cambridge University Press.

Ginja, M. M. D., Silvestre, A. M., & Gonzalo-Orden, J. M. (2010). Diagnosis, genetic control, and preventive management of canine hip dysplasia: a review. The Veterinary Journal.

Harasen, G. (2005). Hip dysplasia in dogs. Canadian Veterinary Journal, 46(11), 1011-1012.

Hasirci, N., & Hasirci, V. N., (2023). Doku Mühendisliği, Hidrojeller ve Biyomürekkepler, 3- Boyutlu Organ Yapımı . Ankara: ODTÜ Yayıncılık.

Herzog, D., Seyda, V., Wycisk, E., & Emmelmann, C. (2016). Additive manufacturing of metals. Acta Materialia, 117, 371-392.

Hollister, S. J. (2005). Porous scaffold design for tissue engineering. Nature Materials, 4(7), 518-524.

Huggard, R., Wicks, G., & Corfield, G. (2022). Short-term clinical assessment of hip hemi-arthroplasty in 11 dogs.

Hummel, D. W., Lanz, O. I., & Werre, S. R. (2020). Complications of cementless total hip replacement. Veterinary and Comparative Orthopaedics and Traumatology.

Kirkby, K. A., & Lewis, D. D. (2012). Canine hip dysplasia: Reviewing the evidence for nonsurgical management. Veterinary Surgery. Wiley Online Library.

Kumar, R., & Reddy, U.K. (2024). The effect of different abutment designs and materials on stress distribution in implants and peripheral bones: A three-dimensional finite element analysis.

Kruth, J. P., Levy, G., Klocke, F., & Childs, T. H. (2010). Consolidation phenomena in laser and powder-bed based layered manufacturing. CIRP Annals, 56(2), 730-759.

Kwananocha, I., Magré, J., Kamali, A., & Verseijden, F. (2024). Outcome one year after acetabular rim extension using a customized titanium implant for treating hip dysplasia in dogs.

Lantada, A. D., & Morgado, P. L. (2012). Rapid prototyping for biomedical engineering: Current capabilities and challenges. Annual Review of Biomedical Engineering, 14, 73-96.

Leary, M., Merli, L., Torti, F., Mazur, M., & Brandt, M. (2018). Optimal design for additive manufacturing: Opportunities and challenges. Materials & Design, 140, 20-32.

Zhang, Y., Liu, X., & Shen, Z. (2024). Evaluation of lattice structures for medical implants. Metals, 14(7), 780.

Li, H., Wang, L., Zhang, H., Gao, Y., & Wu, S. (2016). Titanium and titanium alloys as biomaterials. Advanced Materials Research, 1124, 88-93.

Liu, K., & Tovar, A. (2014). An efficient 3D topology optimization code written in Matlab. Structural and Multidisciplinary Optimization, 50(6), 1175-1196.

Malfair, D., Lavoie, G., Noz, M. E., & DiGioia, A. M. (2015). Precision of radiostereometric analysis (RSA) of acetabular cup stability and polyethylene wear improved by adding tantalum beads to the liner.

Martins, R. S., Germano, M. D., Silva, J. V., & Ribeiro, R. F. (2019). Additive manufacturing in veterinary medicine: A review. International Journal of Advanced Engineering Research and Science, 6(5), 245-254.

Maskery, I., Aboulkhair, N. T., Tuck, C. J., Ashcroft, I. A., & Wildman, R. D. (2018). Compressive failure modes and energy absorption in additively manufactured double gyroid lattices. Additive Manufacturing, 16, 24-29.

Mastrangeli, M., Abbasi, S., Raiteri, R., & Sariola, V. (2015). Drug delivery and biosensing using micro- and nanovibrational systems. Advanced Drug Delivery Reviews, 96, 106-122.

Murphy, S. V., & Atala, A. (2013). 3D bioprinting of tissues and organs. Nature Biotechnology, 32(8), 773-785.

Nebergall, Audrey & Rader, Kevin & Palm, Henrik & Malchau, Henrik & Greene, Meridith. (2015). Precision of radiostereometric analysis (RSA) of acetabular cup stability and polyethylene wear improved by adding tantalum beads to the liner

Pozzi, A., Kowaleski, M. P., & Dyce, J. (2004). Treatment of traumatic coxo-femoral luxation by cemented total hip arthroplasty.

Rafi, H.K., Karthik, N.V., & Gong, H. (2022). Additive manufacturing processes and technologies: Principles, applications, and limitations. Materials Science and Engineering: A, 765, 138262.

Raissi, M., Perdikaris, P., & Karniadakis, G. E. (2019). Physics-informed neural networks: A deep learning framework for solving forward and inverse problems

involving nonlinear partial differential equations. Journal of Computational Physics, 378, 686-707.

Raghuvir, H. B., Shivrajsinh, K. J., Dipak, N. S., & Harit, D. B. (2013). Treatment of canine hip dysplasia: a review.

Rajan, V., Narayan, S., & Shingare, P. D. (2019). Finite Element Analysis and Design of Biomedical Implants. CRC Press.

Reddy, U.K., & Kumar, K.U. (2024). Biomechanical analysis of different implant-abutments interfaces in different bone types: An in silico analysis.

Sing, S. L., An, J., Yeong, W. Y., & Wiria, F. E. (2016). Laser and electron-beam powder-bed additive manufacturing of metallic implants: A review on processes, materials and designs. Journal of Orthopaedic Research, 34(3), 369-385.

Sun, W., Starly, B., Nam, J., & Darling, A. (2018). Bio-CAD modeling and its applications in computer-aided tissue engineering. Computer-Aided Design, 42(7), 635-651.

Taniguchi, N., Fujibayashi, S., Takemoto, M., Sasaki, K., Otsuki, B., Nakamura, T., & Matsushita, T. (2016). Effect of pore size on bone ingrowth into porous titanium implants fabricated by additive manufacturing: An in vivo experiment. Materials Science and Engineering: C, 59, 690-701.

Tomé, I., Alves-Pimenta, S., Sargo, R., & Pereira, J. (2023). Mechanical osteoarthritis of the hip in a one medicine concept: a narrative review.

Torquato, S. (2002). Random Heterogeneous Materials: Microstructure and Macroscopic Properties. Springer.

Vincent, J. F. V., Bogatyreva, O. A., Bogatyrev, N. R., Bowyer, A., & Pahl, A. K. (2006). Biomimetics: Its practice and theory. Journal of the Royal Society Interface, 3(9), 471-482.

Wang, X., Jiang, M., Zhou, Z., Gou, J., & Hui, D. (2021). 3D printing of polymer matrix composites: A review and prospective. Composites Part B: Engineering, 110(4), 442-458.

Warnock, J. J., Dyce, J., Pooya, H., & Schulz, K. S. (2019). Retrospective analysis of canine miniature total hip prostheses. Veterinary Surgery.

Wu, W., Geng, P., Li, G., Zhao, D., Zhang, H., & Zhao, J. (2019). Influence of layer thickness and raster angle on the mechanical properties of 3D-printed PEEK and a comparative mechanical study between PEEK and ABS. Materials, 12(1), 14.

Zhang, Y., Liu, X., & Shen, Z. (2024). Evaluation of lattice structures for medical implants. Metals, 14(7), 780.

Zheng, X., Lee, H., Weisgraber, T. H., Shusteff, M., DeOtte, J., Duoss, E. B., ... & Spadaccini, C. M. (2014). Ultralight, ultrastiff mechanical metamaterials. Science, 344(6190), 1373-1377.

Zienkiewicz, O. C., Taylor, R. L., & Zhu, J. Z. (2013). The Finite Element Method: Its Basis and Fundamentals. Butterworth-Heinemann.